# Quasi-Static Method-of-Moments Modeling of Near-Field Magnetic Coupling in EMI Filter Hardware with Experimental Validation on Multiple PCB Configurations

by

Jenifer Sherrill

A Thesis Presented in Partial Fulfillment

of the Requirements for the Degree

Master of Science

Approved April 2026 by the

Graduate Supervisory Committee:

Ayan Mallik, Chair

Lesley Polka

Antonia Papandreou

ARIZONA STATE UNIVERSITY

May 2026

ABSTRACT

Electromagnetic interference (EMI) filters are critical to achieving conducted-emission compliance in modern power electronic converters. In compact implementations, however, parasitic near-field magnetic coupling between common-mode (CM) and differential-mode (DM) chokes and adjacent capacitor structures can perturb the intended filter response, promote CM-DM mode conversion, and degrade insertion-loss performance. Although these interactions can be captured with high-fidelity electromagnetic solvers, such as full-wave methods or volumetrically discretized partial element equivalent circuit (PEEC) models, those approaches are often computationally prohibitive for rapid iteration across multiple hardware layouts.

This thesis develops a magnetoquasistatic, Method-of-Moments (MoM)-inspired modeling framework for extracting mutual coupling and predicting near-field magnetic field distributions in an EMI filter test printed circuit board (PCB). To reduce computational complexity, the formulation avoids volumetric discretization and instead represents conductive paths as segmented filamentary elements, thereby retaining the dominant inductive interactions governing near-field behavior while significantly reducing memory and runtime requirements. Ferrite cores are incorporated through configuration-specific effective-permeability calibration at 1 MHz, and the common-mode choke is modeled as two explicitly coupled windings on a shared core in order to preserve both CM and DM excitation components. Measured phasor winding currents are used as model inputs, while capacitor-loop currents are obtained through a coupled impedance formulation that captures magnetic interaction between the choke and capacitor network.

The framework is evaluated using four physical PCB configurations in which the chokes are repositioned and reoriented relative to a fixed capacitor network. The resulting coupling matrices and H-field distributions provide quantitative insight into the extent to which component placement and orientation influence coupling strength and spatial field localization. The proposed model therefore serves as a computationally efficient intermediate layer between circuit-level EMI filter synthesis and layout-resolved electromagnetic analysis, while also establishing a foundation for future extensions that incorporate more complete capacitive coupling and PCB power/return-plane effects.

ACKNOWLEDGMENTS

This material is based upon work supported by the National Science Foundation under Grant Number 2236846. I gratefully acknowledge the support of the National Science Foundation in my thesis work.

I would also like to express my sincere gratitude to Connor Reece for his invaluable contributions to this project. Connor was instrumental in the design, procurement, and build of all hardware, including the custom design of the differential-mode choke (DMC), common-mode choke (CMC), and EMI filter printed circuit board (PCB). He defined and constructed the four filter layout configurations, developed and solved the differential-mode (DM) and common-mode (CM) network insertion loss and output impedance circuit models, and established the methodology to extract and provide PEEC solver excitation inputs. Furthermore, Connor defined and implemented the measurement methodologies, collected experimental results, and devised the method to correlate magnetic coupling with effective capacitor equivalent series inductance (ESL) and magnetic choke inductance.

I am deeply grateful to my advisor, Professor Ayan Mallik, for giving me the opportunity to expand my expertise beyond my original skillset in radio frequency (RF) and electromagnetics applications. His guidance and encouragement were essential to my growth and the success of this research.

TABLE OF CONTENTS

Page

LIST OF TABLES

Page

LIST OF FIGURES

Page

# NOMENCLATURE

| Abbreviation | Definition |
|---|---|
| CM | Common Mode |
| DM | Differential Mode |
| CMC | Common-Mode Choke |
| DMC | Differential-Mode Choke |
| EMI | Electromagnetic Interference |
| MoM | Method of Moments |
| PEEC | Partial Element Equivalent Circuit |
| PCB | Printed Circuit Board |
| ESR | Equivalent Series Resistance *(Ω)* |
| ESL | Equivalent Series Inductance *(H)* |
| L | Inductance *(H)* |
| M | Mutual Inductance *(H)* |
| k | Coupling Coefficient *(unitless)* |
| H | Magnetic Field Intensity *(A/m)* |
| B | Magnetic Flux Density *(T)* |

# CHAPTER 1

# INTRODUCTION

## 1.1 Background and Problem Statement

Power electronic converters are increasingly required to achieve high efficiency and power density while meeting stringent electromagnetic compatibility (EMC) requirements. Conducted-emission limits are typically satisfied using electromagnetic interference (EMI) input filters that combine common-mode (CM) and differential-mode (DM) chokes with shunt capacitors. In practice, the attenuation predicted by ideal lumped-element models can be strongly affected by component parasitics and parasitic couplings that arise from the physical layout of inductors, capacitors, and interconnecting PCB planes [1], [2].

In compact EMI-filter assemblies, magnetic coupling between filtering chokes and adjacent current-return paths (including capacitor loops, PCB traces, and nearby power-magnetic components) can shift resonance frequencies, reduce insertion loss, and promote conversion between CM and DM noise (i.e., mode conversion). In practice, CM–DM transformation is typically driven by a combination of non-idealities associated with specific EMI filter components. For example, parasitic inter-winding capacitance—referring to the capacitance between the windings of common-mode (CM) or differential-mode (DM) chokes—can facilitate unwanted coupling between CM and DM signals. Intra-winding capacitance, which is the capacitance within a single winding of a choke, also plays a role in high-frequency behavior and EMI. Capacitor equivalent series inductance (ESL) is another major factor; the ESL of shunt capacitors in the EMI filter can limit their effectiveness at attenuating high-frequency noise, making it essential to select capacitors

with low ESL for optimal filter performance. Additional contributors include stray capacitance to chassis/ground, leakage inductance from imperfect flux cancellation in chokes, mutual coupling between DM and CM filter stages, and asymmetry in layout or terminations. Prior studies have shown that these parasitics and couplings can measurably distort both the conducted-EMI signature and the associated near-field emissions [1], [2], [3], [4], [5].

These coupling mechanisms become increasingly critical for modern high-density and wide-bandgap semiconductor-based power converters, where fast dv/dt and di/dt transitions excite broadband spectral content and increase sensitivity to near-field interactions. For example, near-field coupling between a power loop and a gate-drive loop can corrupt switching waveforms and increase EMI in compact layouts, and magnetic coupling among filtering chokes has been shown to influence conducted EMI in wide-bandgap power-factor-correction systems [6], [7].

Full-wave electromagnetic simulation and detailed Partial Element Equivalent Circuit (PEEC) modeling can capture near-field coupling with high fidelity, but the associated surface/volume discretization and system-matrix sizes can limit iterative use across many candidate layouts. The PEEC framework constructs an equivalent circuit network by extracting partial inductances and resistances, and often capacitances, from a discretized 3-D geometry [8]. This motivates reduced-order quasi-static models that retain the dominant inductive-coupling physics while enabling rapid parametric sweeps and integration with circuit-level design workflows [1], [5], [9].

### 1.1.1 Contributions

This thesis develops and demonstrates the following contributions:

- A segmented-conductor, quasi-static MoM-style impedance formulation for an EMI filter PCB.
- A practical geometry-parameterization workflow based on photo-calibrated component placement.
- Explicit two-winding modeling of the CM choke (L1P and L1N) on a shared core to preserve both CM and DM excitation components.
- Effective permeability calibration at 1 MHz to incorporate ferrite-core behavior without volumetric meshing.
- Field evaluation using a finite straight-segment Biot–Savart formulation to generate H-field maps at probe heights.

Relative to conventional PEEC workflows, the proposed approach retains the circuit-interpretability of partial inductances while emphasizing a MoM-style kernel evaluation and an explicit loop aggregation step. In contrast to volumetric FEA or full-wave MoM solvers, the workflow used in this thesis operates in the magnetoquasistatic (MQS) regime and represents conductors using a reduced set of filament segments and loop currents, which can be exported directly to circuit solvers (e.g., SPICE) as coupled inductors or impedance blocks. This reduced-order formulation enables rapid parametric sweeps of component placement and geometry (using CAD data and photo-calibrated measurements) to quantify how near-field coupling degrades insertion loss and drives CM/DM mode conversion without requiring repeated full 3-D meshing [8], [9], [10].

### 1.1.2 Thesis Organization

Chapter 1 introduces the problem of near-field coupling in EMI filters and summarizes relevant background, including conducted EMI fundamentals, near-field coupling

mechanisms, and prior computational modeling approaches. Chapter 2 presents the proposed quasi-static MoM reduced-order workflow, including geometry parameterization, impedance matrix construction, and excitation/circuit coupling for EMI filter analysis. Chapter 3 describes the experimental hardware configurations and measurement approach used for validation. Chapter 4 presents coupling matrix, H-field distribution, and circuit-level validation results across the four PCB layouts. Chapter 5 concludes and outlines future work.

## 1.2 Conducted EMI and EMI Filter Fundamentals: Near-Field Effects on Performance

This section reviews the physical mechanisms that motivate near-field modeling in EMI filters and summarizes analysis approaches commonly used in power electronics and electromagnetic compatibility (EMC) engineering.

### 1.2.1 Conducted Emissions and EMI Filter Fundamentals

Conducted emissions in power electronic converters are commonly decomposed into differential-mode (DM) and common-mode (CM) components. DM noise appears between the supply and return conductors, whereas CM noise is referenced to chassis or earth and is characterized by current flowing in the same direction on both conductors relative to ground. CM current arises when the two conductors experience similar time-varying potentials with respect to chassis rather than with respect to each other. In practice, this behavior is driven by parasitic capacitances from each conductor to chassis, electromagnetic coupling created by PCB layout and component placement, asymmetry in line and return parasitics that enables DM-to-CM conversion, and fast switching transients that excite poorly controlled return paths. Because the excitation is referenced to ground,

the resulting current returns through chassis or earth and therefore appears as a common-direction current on both conductors.

Practical EMI filters commonly combine a common-mode choke (CMC), a differential-mode choke (DMC), and shunt capacitors to present high impedance to noise currents while preserving the intended power-transfer path. In compact filter assemblies, however, the realized attenuation depends not only on the nominal filter values but also on non-ideal component behavior and layout-dependent parasitics. Magnetic coupling between filtering chokes and adjacent current-return paths, including capacitor loops, PCB traces, and nearby magnetic structures, can modify the effective inductive network seen by the filter. Additional non-idealities such as leakage inductance, inter-winding and intra-winding capacitance, capacitor equivalent series inductance (ESL), and stray capacitance to chassis can shift resonant frequencies, reduce insertion loss, and promote CM-DM mode conversion. As a result, the measured EMI response can deviate significantly from predictions based on ideal lumped-element models [2]– [4].

Reduced-order and fast simulation approaches that incorporate measured or extracted parasitic parameters can improve correlation between filter design intent and measured EMI performance while also supporting sensitivity studies across component tolerances and layout variations [2]. This capability is particularly important when small asymmetries between the positive and negative line parasitics transform DM noise into CM noise, or vice versa, causing seemingly minor layout changes to produce meaningful changes in the conducted-emission signature [3], [4].

Practical filter performance is often quantified using insertion loss (IL), which compares the conducted-noise level with and without the filter under a specified source and load

impedance environment. Because IL depends on both the surrounding impedances and the frequency-dependent non-idealities of real components, accurate prediction requires models that include parasitic elements and coupling paths rather than ideal inductors and capacitors alone [2], [5].

These considerations motivate electromagnetic-aware filter models that retain a circuit representation for efficient system-level analysis while capturing the dominant coupling mechanisms introduced by physical layout. The following section therefore reviews prior work on near-field coupling, parasitic interaction, and DM-CM mode conversion in practical EMI-filter assemblies [1]– [4].

### 1.2.2 Review of Magnetic Near-Field Coupling and Mode Conversion: Challenges and Advances

When inductors and chokes are placed in close proximity, their mutual inductance can become significant relative to the corresponding self-inductance terms, particularly for ferrite-core components with concentrated windings. Under these conditions, magnetic coupling can perturb the effective impedance of each element, redistribute current among adjacent loops, induce conversion between DM and CM paths, and alter the spatial H-field distribution measured above the assembly [5], [7].

Near-field interaction is not limited to passive filter components. In compact converters, coupling between the power commutation loop and sensitive gate-drive or control loops can introduce additional EMI pathways and distort switching behavior. Reduced-order loop-to-loop coupling models are therefore valuable when the switching stage and EMI filter are co-located, since they preserve the dominant magnetic interactions without requiring a full three-dimensional field solution [6].

A substantial body of prior work shows that realistic EMI-filter behavior depends strongly on layout-aware parasitic coupling. Murata et al. demonstrate that coupling among filter capacitors can shift resonances and modify insertion loss, indicating that coupling is often a first-order design variable rather than a secondary perturbation at high frequency [1]. Wang et al. similarly report that coupling between the common-mode choke and nearby capacitors, as well as winding orientation within the choke, materially affects filter performance [2]. Taken together, these studies show that practical EMI filters must be modeled as interacting electromagnetic assemblies rather than as collections of isolated lumped elements [1], [2].

Magnetic coupling among inductive components can be equally important. McGrew et al. show that, in a GaN-based power-factor-correction converter, the boost-inductor air gap can modify the coupling between the boost inductor and the differential-mode filter inductance, effectively creating an additional parallel coupling path that degrades both DM and CM attenuation [7]. For the present work, this result motivates explicit extraction of mutual inductance terms between EMI-filter loops as a function of physical layout. Rather than performing a full three-dimensional electromagnetic solve for every configuration, this thesis constructs a compact loop-inductance matrix whose off-diagonal terms quantify layout-dependent coupling directly [7].

Measurement-based and simulation-based approaches have both been used to study these phenomena. Near-field magnetic scanning with small-loop H-field probes and magnetic-moment analysis has been used to localize dominant emission sources and assess field-reduction techniques for inductors and power-electronic subsystems [11], [12]. These approaches are especially informative for toroidal inductors and common-mode chokes,

whose leakage-field distributions can vary substantially with winding symmetry and mounting orientation [11], [12]. Complementing measurement, PEEC-based extraction and other three-dimensional electromagnetic solver approaches are commonly used to quantify leakage fields and mutual inductive coupling into nearby loops [8].

Mode conversion provides another important mechanism by which practical EMI filters deviate from idealized behavior. Wang and Lee show that asymmetries in component values and layout can couple DM and CM networks that are ideally independent [3]. Roudposht et al. extend this perspective with circuit-modeling approaches for non-ideal EMI filters, emphasizing that imbalance and parasitic coupling create cross-mode transfer paths that must be represented explicitly in multi-loop or multi-port models [4]. These results motivate the explicit separation of line and neutral winding paths in coupled models, rather than representing a common-mode choke as a single idealized element [3], [4].

A broader review by Jie et al. further emphasizes that practical EMI-filter chokes exhibit multi-resonant behavior and coupling effects that vary with frequency, winding arrangement, and termination [5]. This literature supports the use of compact models that preserve the dominant coupling physics while remaining computationally trace for filter-level simulation and layout optimization [5].

### 1.3 Review of Computational Methods for Near-Field Coupling

Circuit-level models enable rapid design iteration, but they require parasitic quantities such as mutual inductance, stray capacitance, and loop resistance to be known a priori. On the opposite extreme, full-wave electromagnetic solvers can directly resolve field distributions and coupling between structures, but they generally require fine surface or volumetric

meshes, large system matrices, and long runtimes when applied to electrically small yet geometrically detailed power-electronic hardware. Between these extremes, the Partial Element Equivalent Circuit (PEEC) method provides a useful compromise by transforming a discretized conductor geometry into a circuit-compatible network of partial inductances, resistances, and, when included, capacitance coefficients. In this way, PEEC preserves geometry-dependent electromagnetic coupling while remaining compatible with external circuit simulators [8], [9].

Table 1.1 compares the numerical approaches most used for low-frequency near-field analysis in power-electronic converters. The appropriate method depends on the modeling objective. Full-wave methods are valuable when radiation, broadband behavior, or detailed internal field distributions in magnetic and dielectric materials must be resolved. In contrast, quasi-static and reduced-order methods are often preferable when the primary objective is rapid extraction of layout-dependent parasitics for EMI-filter design and iteration.

Table 1.1: Comparison of Computational Methods for Low-Frequency Near-Field Analysis in Power-Electronic Converters.

| Numerical computation method | Representative software | What it solves | Power-converter applications | Main limitations |
|---|---|---|---|---|
| PEEC / Quasi-Static MoM | FastHenry, FastCap, Ansys Q3D | Extracts circuit-compatible partial L, R, and optionally C terms or impedance/coupling matrices from discretized conductors; well suited to MQS parasitic extraction. | EMI filters, busbars, PCB traces, winding structures, cable/interconnect parasitics, rapid comparison of layout-dependent mutual coupling. | Most accurate when the structure is electrically small and radiation is negligible; dense matrices and model size increase with discretization. |
| Surface MoM (Full-Wave) | Keysight Momentum, Altair FEKO | Solves surface currents on metallic structures in open regions; useful for S-parameters, mutual coupling, radiation, and CM-DM conversion on PCBs/cables. | Open-board structures, cables, interconnects, higher-frequency coupling studies. | Dense full-wave matrix; less suitable when internal fields in ferrites or dielectrics must be resolved. |
| Low-Frequency / Quasi-Static FEM | Ansys Maxwell | Solves magnetostatic and eddy-current fields | Ferrite cores, transformers, chokes, motors, | Requires 3-D volume meshing of |

| Numerical computation method | Representative software | What it solves | Power-converter applications | Main limitations |
|---|---|---|---|---|
| | | in volumetric magnetic materials and surrounding air; captures flux concentration, leakage fields, and core behavior. | magnetic-component field mapping. | both material and air region; typically solved one frequency or operating point at a time. |
| FEM (edge-element, full-wave) | Ansys HFSS, CST EM Studio | Full-wave 3-D solution of Maxwell's equations in complex structures containing conductors, dielectrics, and magnetic materials. | Detailed internal-field studies of packages, resonant structures, connectors, and mixed-material assemblies. | Large air-box and fine volumetric mesh requirements; memory- and time-intensive for full converter assemblies. |
| FDTD (time-domain) | openEMS, CST Time-Domain, Ansys EMA3D | Time-domain field solution on a spatial grid; captures transients and broadband spectra in a single simulation. | Switching transients, broadband EMI, enclosure/cable interactions, wideband conducted/radiated studies. | Large computational domain, small cell sizes for fine features, time-step stability constraints, and long runtimes for detailed low-frequency systems. |
| Circuit + RLGC extraction / SPICE models | SPICE-based tools | Represents interconnects and components as lumped or distributed R-L-C-G networks. | Fast system-level analysis of filters, harnesses, and interconnects when only parasitic values are needed. | Does not directly resolve fields; accuracy depends on extracted or fitted parasitics; limited for distributed-wave and |

| Numerical computation method | Representative software | What it solves | Power-converter applications | Main limitations |
|---|---|---|---|---|
| | | | | radiation effects. |

For the low-MHz conducted-EMI problems considered in this thesis, the relevant behavior lies firmly within the near-field and electrically small regime. The reactive near-field boundary may be approximated by $r \lesssim \lambda/2\pi$. At $f = 1\,\text{MHz}$, $\lambda \approx 300\,\text{m}$, so $\lambda/2\pi \approx 48\,\text{m}$, which is orders of magnitude larger than both the dimensions of the EMI-filter PCB and the probe heights used in this work ($z \approx 13$–$35\,\text{mm}$). Under these conditions, radiation effects are negligible, and the dominant physics are magnetoquasistatic (MQS): mutual inductive coupling, current redistribution among nearby loops, and common-mode/differential-mode interaction [9].

PEEC is particularly relevant in this regime. In its classical form, PEEC discretizes conductors into surface or volume cells and represents their interactions through an equivalent circuit composed of partial inductances, resistances, and coefficients of potential [8]. Because the formulation is closely related to integral-equation and Method-of-Moments (MoM) viewpoints, the extracted network can be solved using circuit techniques while still preserving geometry-dependent electromagnetic coupling [8], [9]. Although PEEC can be extended toward retarded or full-wave formulations by incorporating radiation and propagation effects, those extensions increase model order and computational cost and are therefore less attractive for rapid EMI-filter layout exploration in the low-MHz regime [8].

In practice, the computational cost of PEEC depends strongly on the chosen discretization. Surface- and volume-based representations are often necessary when internal field distributions, charge storage effects, or complex three-dimensional magnetic geometries must be captured in detail. However, these representations can produce large dense matrices and long solve times when many PCB configurations must be evaluated. Detailed treatment of PCB traces, vias, component leads, and magnetic structures can therefore become prohibitively expensive for iterative layout studies.

For low-frequency EMI-filter design, it is advantageous to exploit MQS conditions and focus on the dominant current-carrying paths. This motivates reduced-order formulations in which currents are represented by filamentary or surface-current basis functions along the conductors of interest, rather than by volumetric meshing of the entire conductor body. Such approaches retain the MoM-style coupling physics most relevant to near-field EMI behavior while substantially reducing the number of unknowns [8], [9].

The reduced-order model adopted in this thesis follows this logic. Instead of discretizing the full conductor volume, the choke windings and capacitor return paths are represented by filamentary basis elements aligned with the dominant current trajectories. This yields a compact impedance and mutual-inductance representation that preserves the layout-dependent inductive interactions governing near-field coupling, while remaining computationally efficient enough for repeated evaluation of multiple PCB configurations. As a result, the model provides a practical bridge between circuit-level EMI-filter analysis and layout-resolved electromagnetic design [8], [9].

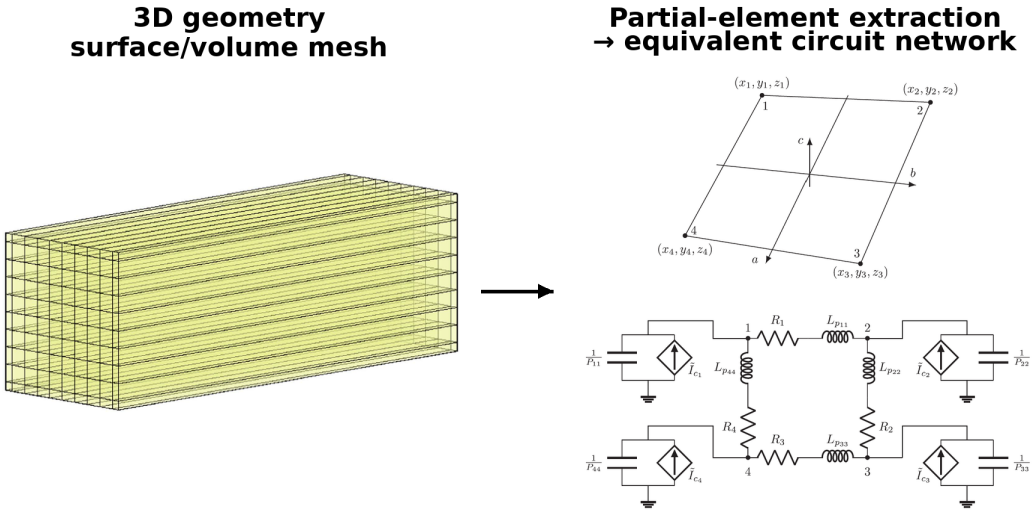


Figure 1.1: Conceptual PEEC extraction process: a 3-D electromagnetic geometry is discretized into conductor elements, partial electromagnetic quantities are computed between the elements, and the extracted $\boldsymbol{R}$, $\boldsymbol{L}$, and $\boldsymbol{C}$ coefficients are mapped into an equivalent circuit network suitable for circuit-level simulation [17].

### 1.3.1 Motivation for a Reduced-Order, Layout-Aware Model

For EMI-filter layout exploration, the design questions are frequently comparative: how does moving a choke, rotating a core, or swapping the mounting orientation change mutual coupling and near-field emissions? Prior work on parasitic parameters and parasitic couplings in EMI filters shows that these layout-dependent interactions can significantly

alter filter behavior [1], [2]. Answering such questions with a full PEEC or full-wave finite element analysis (FEA) tool can be burdensome because it requires a new mesh and a new solve for each layout perturbation, motivating lighter-weight models for design iteration.

Answering such questions with a full PEEC or volumetric finite-element model can be burdensome because each layout perturbation generally requires regeneration of the discretization and re-solution of the field problem. Finite-element analysis (FEA) and other three-dimensional field solvers can resolve skin effect, proximity effect, and complex material responses with high fidelity, but they do so by solving large algebraic systems derived from volumetric meshes. For linear material models, each new geometry, frequency point, or boundary-condition change requires assembly and solution of a new system. For nonlinear magnetic materials, additional iterations are required because constitutive properties such as permeability depend on the local field solution, so the material state and field solution must be updated until convergence is reached.

Although this level of fidelity is valuable when conductor cross-sectional current redistribution or detailed core physics must be resolved, it is poorly matched to the design task considered here: rapid comparison of multiple EMI-filter layouts to determine how translation, rotation, and relative placement alter mutual coupling and near-field behavior. Even when advanced solvers such as Maxwell or HFSS are used successfully, parametric sweeps remain expensive because mesh refinement around small features, air-region meshing, and repeated frequency- or configuration-specific solves substantially increase runtime and memory requirements. This motivates reduced-order integral-equation formulations, including PEEC- and MoM-based approaches, that preserve the dominant

inductive coupling mechanisms while dramatically reducing the number of unknowns under MQS conditions [8], [9].

Prior work further shows that magnetic coupling does not merely shift resonance frequencies; it can also create effective bypass paths that directly reduce the intended filter impedance. In the GaN-based PFC converter study of McGrew et al., coupling associated with a nearby inductor air gap effectively introduced a parallel path with the intended differential-mode inductance, thereby reducing attenuation [7]. Together with prior EMI-filter studies on parasitic coupling [1], [2], this result indicates that mutual inductance should be treated as a primary, layout-dependent design parameter during filter placement and orientation studies [1], [2], [7].

The model developed in this thesis adopts a Method-of-Moments (MoM)-inspired discretization of the dominant current paths using thin-wire filament segments [9]. Rather than volumetrically meshing the full PCB and ferrite cores, the conductors are represented by a compact set of centerline segments, while ferrite effects are incorporated through an effective-permeability calibration consistent with common modeling practice for EMI-filter chokes [5]. This representation enables rapid recomputation of mutual coupling under choke translation and rotation while remaining consistent with the magnetoquasistatic assumptions adopted at 1 MHz [9].

Relative to conventional PEEC implementations, the proposed approach emphasizes three features. First, the dominant current paths are discretized using filamentary basis elements rather than a full surface or volumetric mesh. Second, the common-mode choke is represented explicitly as two windings, $L_{1P}$ and $L_{1N}$, so that winding currents can be

applied or identified directly. Third, the solved loop currents are used directly in a Biot–Savart post-processing step to predict near-field magnetic-field distributions. These choices prioritize computational efficiency and physical interpretability over exhaustive representation of conductor cross-sectional and dielectric detail. Cross-sectional current redistribution due to skin and proximity effects is absorbed into effective self-resistance terms, distributed capacitance is neglected because the present model is focused on low-frequency inductive coupling, and radiation is excluded because the structures are electrically small over the frequency range of interest. This reduced-order viewpoint is therefore well suited to early-stage EMI-filter layout optimization, where relative coupling trends and mode-conversion pathways are the primary design objectives [8], [9], [12].

Conceptually, PEEC and filament-based inductive extraction share the same integral-equation foundation. Both begin by discretizing electromagnetic interactions into matrix form using MoM principles. In classical PEEC, this discretization produces partial inductances and coefficients of potential associated with volumetric or surface cells. In the reduced-order formulation adopted here, the basis elements are line segments aligned with the dominant conductor paths, and the resulting segment interactions are aggregated into a smaller loop-inductance matrix that is more convenient for circuit simulation [8], [9].

The numerical advantage of this reduced-order filament/MoM representation is reflected directly in the number of unknowns. A volumetric 3-D PEEC or FEA model of an EMI-filter inductor must typically resolve conductor cross-sections, nearby dielectrics, air regions, and small geometric gaps, which can readily produce on the order of $10^3$ to $10^6$ field unknowns, depending on operating frequency and geometric detail. By contrast, a

filament model may represent each winding with on the order of $10^2$ current segments, after which loop aggregation compresses the unknowns further to on the order of 10 loop currents while retaining the dominant mutual-inductance couplings. As a representative example, discretizing a two-winding choke with approximately 200 segments per winding yields roughly 400 segment-current unknowns; grouping those segments into a small number of loop variables then provides an order-of-magnitude reduction for the subsequent circuit solve and for repeated parametric sweeps [8], [9].

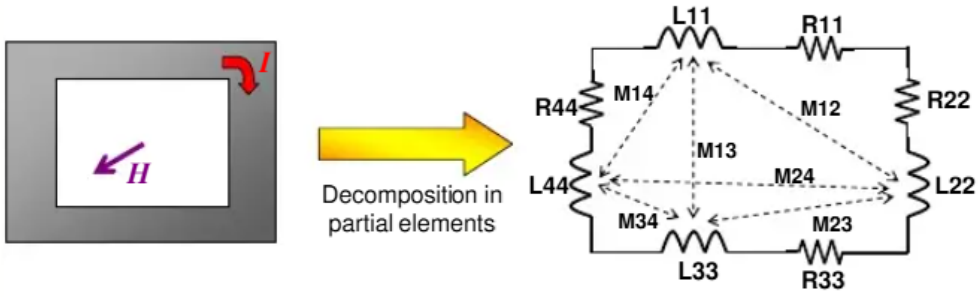


Figure 1.2: Partial-element decomposition of a rectangular conductor loop, illustrating how physical geometry can be represented by localized resistance, self-inductance, and mutual-inductance elements [16].

Beyond the computational distinction illustrated in Fig. 1.2, layout asymmetries and parasitic couplings can also mediate mode conversion between differential-mode (DM) and common-mode (CM) currents. The DM/CM decomposition provides a convenient

modal framework for interpreting conducted-noise mechanisms by recasting a two-conductor system in terms of anti-phase (DM) and in-phase (CM) voltage and current components. Within this framework, transformation matrices and modal network formulations relate two-port measurements to DM/CM impedances and insertion loss, thereby clarifying how imbalance and parasitic interaction redistribute energy between the two modes [3]. More recent studies have shown that coupling within the filter assembly, and between the filter and adjacent power-stage loops, can drive DM-to-CM conversion and thereby alter both conducted-emission signatures and the associated magnetic-field distributions, particularly in compact wide-bandgap converter layouts where magnetic components are tightly packed [4], [6].

Because the measured near-field magnetic pattern is governed by the same underlying loop-current distribution, mutual-inductance extraction can be used not only for circuit-level interpretation but also for field prediction. For example, mutual-inductance-based methods have been used to quantify coupling between integrated power converters and nearby passive components as a function of separation and orientation, thereby creating a direct link between geometric changes and EMI behavior [13]. This observation motivates the workflow adopted in this thesis: for each candidate layout, a physically based coupling matrix is extracted once and then reused to evaluate both circuit-level performance metrics, such as insertion loss and output impedance, and spatial near-field quantities derived from the solved loop currents [6], [7].

### 1.3.2 Summary and Research Gap

The literature reviewed above establishes three central points. First, parasitic coupling and component non-idealities can materially alter EMI-filter behavior by shifting resonant frequencies, degrading insertion loss, and enabling conversion between differential-mode (DM) and common-mode (CM) currents [1]– [5]. Second, these interactions are strongly dependent on physical geometry: component placement, orientation, return-path structure, and proximity between magnetic and capacitive elements all influence both circuit-level response and the spatial distribution of the near magnetic field [1], [2], [6], [7], [11]– [13]. Third, existing high-fidelity computational methods, including PEEC, finite-element analysis, and other three-dimensional field solvers, can capture these effects with substantial detail, but their computational cost often makes them impractical for rapid evaluation of many candidate hardware configurations [8], [9].

What remains insufficiently addressed in the literature is not the existence of electromagnetic extraction methods themselves, but the lack of a workflow specifically tailored to EMI-filter layout exploration in the low-MHz magnetoquasistatic regime. In particular, prior work does not fully close the gap between layout-aware electromagnetic modeling and design-oriented filter analysis. A practical methodology is needed that can *(i*) parameterize as-built EMI-filter hardware from CAD data or calibrated photographs, (*ii)* preserve the physically important separation between the two common-mode choke windings and the dominant capacitor return loops, (*iii*) extract self- and mutual-inductance terms in a form that remains directly interpretable at the circuit level, and (*iv*)

reuse that same reduced representation to predict both circuit-domain behavior and spatial near-field magnetic distributions across multiple layouts [3]–[9], [11]–[13].

The research gap addressed in this thesis is therefore a configuration-driven, layout-aware, and computationally efficient modeling framework that remains grounded in electromagnetic first principles while avoiding the cost of repeated full three-dimensional meshing. Rather than resolving every geometric and material detail through a volumetric field solve, the proposed approach focuses on the dominant current paths that govern near-field magnetic interaction in compact EMI-filter assemblies. These paths are represented using a reduced-order, Method-of-Moments-inspired filament discretization, ferrite effects are incorporated through an effective-permeability calibration at 1 MHz, and the resulting coupled system is solved in terms of compact loop currents and loop inductances. The output is not simply a numerical prediction of filter response; it is a physically interpretable coupling matrix together with near-field $H$-field maps that reveal how translation, rotation, and relative component placement modify the dominant interaction pathways [5], [8], [9].

A second gap addressed by this work concerns validation and reuse. Much of the prior literature emphasizes either component-level field characterization, circuit-level parasitic modeling, or high-fidelity numerical extraction in isolation. By contrast, the framework developed here is intended to operate as an intermediate layer between circuit design and layout-resolved electromagnetic analysis. The same extracted coupling representation is reused to support comparison across multiple PCB configurations and to connect geometric variation to both circuit-level figures of merit and spatial magnetic-field

behavior. In this sense, the contribution of the thesis is not merely a reduced-order solver, but an integrated modeling workflow for EMI-filter layout studies that balances physical interpretability, computational efficiency, and experimental relevance. The following chapter develops the proposed formulation in detail and describes the experimental validation strategy used in this work.

# CHAPTER 2

# QUASI-STATIC METHOD-OF-MOMENTS MODELING METHODOLOGY

This chapter presents the reduced-order modeling framework developed to extract coupling parameters and predict near-field magnetic-field distributions for the EMI-filter PCB studied in this thesis. The hardware consists of one common-mode choke, two differential-mode chokes, and multiple capacitor structures arranged on a compact printed circuit board. The formulation operates in the magnetoquasistatic regime and is inspired by integral-equation and Method-of-Moments (MoM) discretization concepts, but it is implemented in a reduced-order form suitable for rapid comparison of multiple layout configurations [8], [9].

Although the field solution is obtained using a quasi-static MoM-style formulation, the resulting self- and mutual-impedance terms remain consistent with the Partial Element Equivalent Circuit (PEEC) viewpoint. In particular, each discretized conductor segment can be interpreted as a partial element, and the assembled impedance matrix maps directly to an equivalent circuit representation that can be exported to a circuit solver for EMI-filter performance analysis. This interpretation preserves the physical meaning of the extracted coupling terms while avoiding the computational cost associated with full volumetric meshing and repeated three-dimensional field solves [8], [9].

Figure 2.1 summarizes the reduced-order workflow used throughout this thesis. The process begins with parameterization of the physical layout, including component locations, loop geometries, and observation-plane definitions. The dominant current paths are then discretized into filament segments and grouped into electrical loops through an

incidence matrix B. A MoM-style inductive kernel is evaluated to assemble the segment-level impedance terms, including partial inductive coupling and resistance contributions. These segment quantities are then aggregated into a loop-level impedance matrix, enabling a compact circuit solution for both the known excitation currents and the induced loop currents. Finally, the solved loop currents are used in a Biot-Savart post-processing step to generate near-field H-field maps for comparison with measured scan data [8], [9], [12].

Figure 2.1. Reduced-order MoM-style modeling workflow used in this thesis: geometry parameterization, filament discretization, segment-level kernel evaluation, loop aggregation, and circuit/field post-processing.

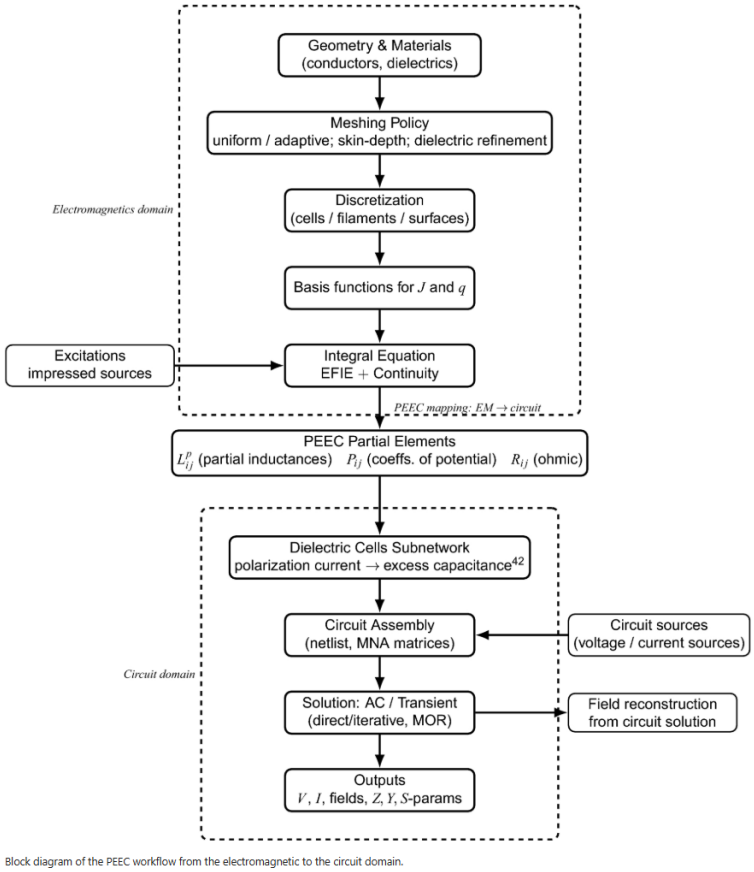


Block diagram of the PEEC workflow from the electromagnetic to the circuit domain.

Figure 2.1: Reduced-order MoM-style modeling pipeline implemented in this thesis. Physical EMI filter geometry is converted into a discretized conductor representation, electromagnetic coupling terms are extracted, and the resulting reduced-order circuit model is solved for terminal behavior and predicted near-field quantities [15].

## 2.1 Geometry Parameterization and Configuration

The EMI-filter layout is parameterized in a board-fixed coordinate system. For comparison across configurations and with measured field scans, the analysis focuses on the 80 mm x 90 mm region containing the chokes and capacitor network. In each configuration, each choke is described by its center position and an orientation vector referenced to the board coordinate axes. These quantities may be obtained directly from CAD data or estimated from calibrated photographs using the PCB grid as a spatial reference.

Each winding and capacitor return path is modeled as a closed filamentary path composed of straight segments. A multi-turn winding is represented by stacking successive loop revolutions along the toroidal axis using an axial pitch consistent with the wire diameter and observed fill factor. This discretization corresponds to a thin-wire pulse-basis / point-matching Method-of-Moments (MoM) representation, which is well suited to magnetoquasistatic (MQS) extraction of inductive coupling [9].

Ferrite-core effects are incorporated without volumetric meshing. Instead, each core is represented through a configuration-specific effective permeability, $\mu_{eff}$, calibrated at 1 MHz so that the modeled self-inductance matches the measured or target inductance:

$$\mu_{\text{eff}} = \mu_{\text{nom}} \frac{L_{\text{target}}}{L_{\text{model}}} \qquad (2.1)$$

where $\mu_{nom}$ is the nominal or datasheet permeability, $L_{target}$ is the measured or target inductance at 1 MHz, and $L_{model}$ is the inductance predicted by the filament model using $\mu_{nom}$. This calibration preserves the computational efficiency of the reduced-order filament model while approximately accounting for ferrite loading at the operating frequency.

Unlike simplified common-mode choke (CMC) models that enforce purely common-mode excitation, the proposed model represents the CMC as two explicit windings, $L_{1P}$ and $L_{1N}$ , wound on a shared core. This permits direct application of the measured phasor current in each winding and preserves both common-mode and differential-mode excitation components. The shared-core coupling between the two windings is retained through the impedance formulation, which is important for capturing imbalance-driven mode-conversion pathways [3], [5].

After geometry parameterization, a segment-level inductance matrix is assembled from pairwise filament interactions. Under MQS assumptions, the mutual inductance between filament segments m and n is evaluated using a Neumann-type partial-inductance kernel [8], [9]:

$$L_{mn} = \frac{\mu_0}{4\pi} \int_{\ell_m} \int_{\ell_n} \frac{d\ell_m \cdot d\ell_n}{R_{mn,\text{eff}}} \qquad (2.2)$$

where $d\ell_m$ and $d\ell_n$ are differential tangent vectors along segments $m$ and $n$, respectively, and $R_{mn,eff}$ is the regularized separation distance between the corresponding differential elements. In the present reduced-order implementation, ferrite loading is incorporated through the effective-permeability calibration described above rather than through volumetric core meshing.

For time-harmonic excitation at angular frequency ω, the inductive contribution to the segment impedance matrix is

$$Z_{mn}^{(L)} = j\omega L_{mn} \qquad (2.3)$$

Because the present formulation is magnetoquasistatic and inductive, capacitance coefficients and radiation terms are not included in this subsection.

The segment impedance matrix is then written as

$$\mathrm{Z_{seg}}(\omega) = \mathrm{R_{ac}}(\omega) + j\omega \mathrm{L_{seg}} \qquad (2.4)$$

and the segment voltages and currents satisfy

$$\mathrm{V_{seg}} = \mathrm{Z_{seg}}(\omega)\mathrm{I_{seg}} \qquad (2.5)$$

where contains only diagonal AC-resistance terms in the present work. Mutual resistance terms and detailed proximity-effect coupling are therefore neglected in this reduced-order formulation.

To prevent singular or ill-conditioned evaluations when adjacent segments are very closely spaced, the separation distance in Eq. (2.2) is regularized as:

$$R_{mn,\text{eff}} = \max\left(R_{mn}, R_{min}\right) \qquad (2.6)$$

where $R_{mn}$ is the physical separation between the differential length elements and $R_{min}$ is a prescribed minimum distance.

Segment quantities are mapped to loop quantities through a segment-to-loop incidence matrix $\mathrm{B} \in \{-1,0,+1\}^{N_{\text{seg}} \times N_{\text{loop}}}$ ,whose entries encode loop membership and segment orientation. In practice, B is constructed by assigning each segment a loop identifier and an orientation sign: +1 if the segment direction matches the loop traversal direction, -1 if it opposes the loop traversal direction, and 0 otherwise. Using $I_{seg} = BI_{loop}$ and $V_{loop} = B^T V_{seg}$, the aggregated loop inductance and resistance matrices are

$$L_{loop} = B^T L_{seg} B \qquad (2.7)$$

$$R_{loop} = B^T R_{ac} B \qquad (2.8)$$

and the corresponding loop impedance matrix becomes

$$Z_{loop}(\omega) = R_{loop}(\omega) + j\omega L_{loop} \qquad (2.9)$$

For loop groups *i* and *j* , the mutual inductance is obtained as

$Mij = [L_{loop}]ij$,

and the corresponding coupling coefficient is defined as

$$k_{ij} = \frac{M_{ij}}{\sqrt{[L_{loop}]ii[L_{loop}]jj}}.$$

This aggregation yields compact loop-level parameters that are directly usable in the reduced circuit model and in comparative layout studies [5], [8].

Figure 2.2 highlights two key operations in the proposed formulation. First, the Neumann kernel is evaluated for each filament-segment pair to populate the dense segment inductance matrix $L_{seg}$ (left). Second, the segment matrix is projected into a much smaller loop-inductance matrix via the incidence mapping

$L_{loop} = B^T \cdot L_{seg} \cdot B$ (right),

so that each loop self-inductance and mutual-inductance term reflects the aggregate effect of many underlying segment interactions. This loop aggregation is central to reducing computational cost while preserving the dominant coupling pathways needed for circuit prediction and near-field evaluation [8], [9].

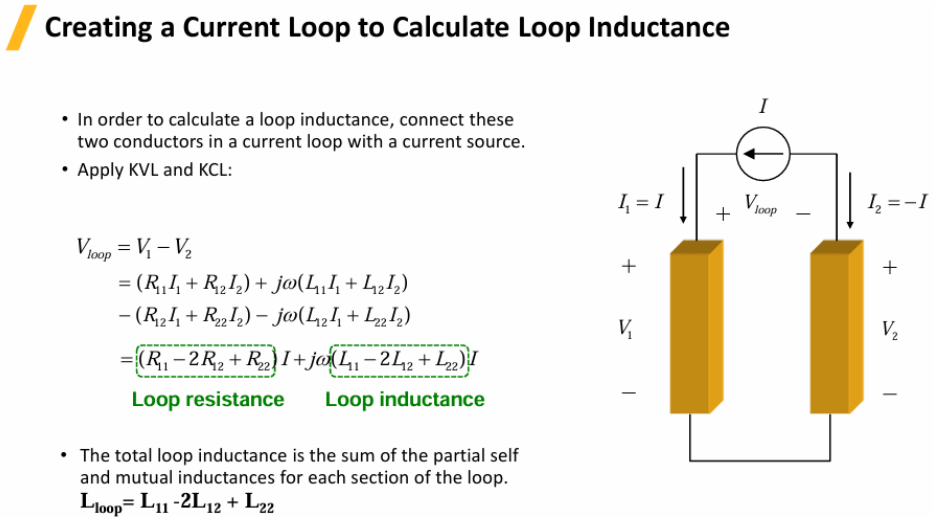


Figure 2.2: Formation of loop inductance from partial self- and mutual-inductance terms. Partial segment-level

inductance contributions are combined by enforcing a current loop, yielding the reduced loop-inductance quantity used in the circuit-domain model [14].

Given measured phasor currents for the choke windings, these loops are treated as known current excitations in the reduced-order circuit model. The remaining passive loop currents are then obtained from the coupled loop-impedance system. Partitioning the loop set into known loops *k* and unknown loops *u*, the frequency-domain loop equations may be written as:

$$\begin{bmatrix} \mathrm{V}_k \\ 0 \end{bmatrix} = \begin{bmatrix} \mathrm{Z}_{kk} & \mathrm{Z}_{ku} \\ \mathrm{Z}_{uk} & \mathrm{Z}_{uu} \end{bmatrix} \begin{bmatrix} \mathrm{I}_k \\ \mathrm{I}_u \end{bmatrix} \qquad (2.10)$$

where $\mathrm{I}_k$ contains the measured phasor currents applied to the driven choke windings, $\mathrm{I}_u$ contains the unknown currents in the passive loops, and passive loops have zero impressed voltage. Solving the second block row for the unknown loop currents gives:

$$\mathrm{I}_u = -\mathrm{Z}_{uu}^{-1}\mathrm{Z}_{uk}\mathrm{I}_k \qquad (2.11)$$

The corresponding driving voltages are then recovered from the first block row as

$$V_k = (Z_{kk} - Z_{ku}Z_{uu}^{-1}Z_{uk})I_k$$

This partitioned formulation enables direct use of measured current excitation while preserving the mutual coupling between the driven choke windings and the remaining loops in the reduced-order network [4], [5].

Near-field evaluation is performed using the finite-segment Biot–Savart law to compute the magnetic-field intensity $H$ on the measurement plane. The total field is obtained by summing the contributions of all current-carrying segments in the modeled loop network. For a straight segment $m$, the field contribution is written as:

$$H(r) = \sum_m H_m(r), H_m(r) = \frac{I_m}{4\pi} \frac{\mathrm{u}_m \times \mathrm{R}_{\perp,m}}{\|\mathrm{R}_{\perp,m}\|^2} \left[ \frac{s_{2,m}}{\sqrt{\|\mathrm{R}_{\perp,m}\|^2 + s_{2,m}^2}} - \frac{s_{1,m}}{\sqrt{\|\mathrm{R}_{\perp,m}\|^2 + s_{1,m}^2}} \right] \quad (2.12)$$

where $I_m$ is the current in segment $m$, $\mathrm{u}_m$ is the unit vector along the segment direction, $\mathrm{R}_{\perp,m}$ is the perpendicular displacement vector from the segment line to the observation point, and $s_{1,m}$ and $s_{2,m}$ are the signed distances from the perpendicular projection point to the two segment endpoints. For numerical stability, the magnitude $\| \mathrm{R}_{\perp,m} \|$ is regularized using a minimum distance $R_{\min}$ when the evaluation point lies very close to a conductor. This expression yields the vector magnetic-field intensity in A/mand is used to generate the predicted scan-plane field maps for comparison with measured H-field distributions.

In this thesis, magnetoquasistatic approximation is justified because the electrical size of the structure is small. A common sufficient condition is:

$$\begin{aligned} k_0 L_{\max} &\ll 1, \\ k_0 &= \frac{2\pi}{\lambda} = \frac{2\pi f}{c} \end{aligned} \quad (2.13)$$

where $L_{max}$ is the maximum physical dimension of the structure, $\lambda$ is the wavelength at frequency $f$, and $c$ is the speed of light. At 1 MHz, $\lambda \approx 300$ m. Taking $L_{max} \approx 0.10$ m for the present PCB-scale structure gives $L_{max} / \lambda/10 \approx 3.3 \times 10{-}4$ and $k_0 L_{\max} \approx 2.1 \times 10^{-3} \ll 1$.

Under these conditions, retardation and radiation effects are negligible, and static inductive kernels provide an appropriate approximation for the near-field interactions of interest.

From a numerical standpoint, thin-wire formulations can become ill-conditioned when segment separations are very small or when nearly coincident segments occur in the discretization. The implementation therefore uses two stabilization measures: *(i)* minimum-distance regularization in the Neumann and Biot-Savart evaluations, and *(ii*) a small diagonal perturbation when the loop-impedance system becomes ill-conditioned. The diagonal stabilization is applied as:

$$\tilde{Z} = Z_{loop} + \epsilon I, \, if \, rcond\,(Z_{loop}) < \tau \tag{2.14}$$

where $\varepsilon$ is a small positive scalar and $I$ is the identity matrix, and $\tau$ is a prescribed reciprocal-condition-number threshold. These steps improve numerical stability without materially affecting the solved loop currents or the near-field distributions on the measurement planes considered.

Figure 2.3 summarizes both the physical and numerical justification for the MQS model. On the physical side, the filter dimensions and probe heights lie far below $\lambda/2\pi$ at 1 MHz, so inductive near-field coupling dominates over radiated far-field behavior. On the numerical side, the figure also emphasizes the regularization controls, including the minimum separation distance $R_{min}$, symmetry enforcement, and conditional diagonal stabilization, that prevent singular or poorly conditioned kernel evaluations when

computing self and near-neighbor terms. These controls improve stability without materially altering the coupling trends at the distances of interest.

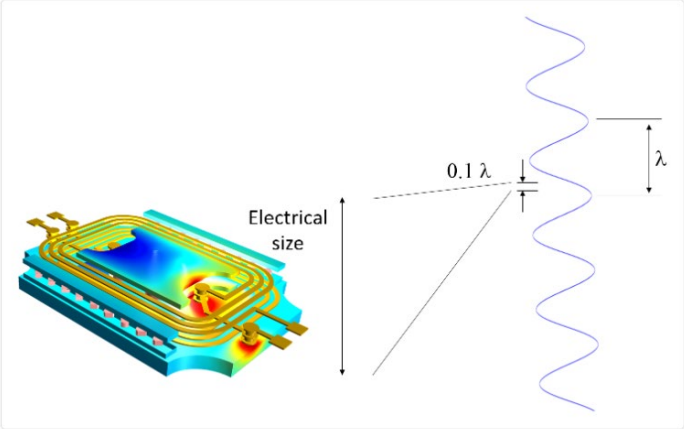


Figure 2.3: Magnetoquasistatic operating regime used for the reduced-order EMI filter model. The quasistatic approximation is appropriate when the characteristic filter dimension is much smaller than the electromagnetic wavelength, allowing retardation and radiation effects to be neglected in the coupling model. Adapted from COMSOL, Introductory Guide to Field Electromagnetics and Theory, “Magnetoquasistatics” and electromagnetic wavelength-regime diagram

For each PCB configuration, the model produces *(i)* an 8×8 loop-inductance matrix containing self-inductances and mutual inductances among the two common-mode choke windings, the two differential-mode chokes, and four capacitor loops; *(ii)* derived coupling coefficients $k_{ij}$; and *(iii)* near-field *H*-maps at user-specified probe heights for both *DM* and *CM* excitation cases. These outputs are exported to MATLAB .mat files and CSV tables to support circuit-level analysis and comparison against experimental measurements.

## 2.2 Circuit-Level Metrics and Mutual Coupling Integration

The starting point is a full parasitic lumped-element network in which each passive component is represented by an ideal element together with its dominant high-frequency parasitics, including equivalent series resistance (ESR), equivalent series inductance (ESL), and, where appropriate, equivalent parallel resistance and equivalent parallel capacitance. The network is organized in the mode domain: a balanced CLC ($\pi$-type) stage represents the differential-mode (DM) filtering path, whereas a balanced LC stage represents the common-mode (CM) path to chassis or ground. Within this framework, mutual inductances are not treated as small perturbative corrections. Instead, they appear as off-diagonal terms that couple the inductive branches of the assembled filter, including the choke windings and capacitor return loops.

The reference ESL values correspond to the nominal capacitor parasitics, whereas the configuration-specific effective ESL values are derived from the extracted loop-inductance matrix to capture the effect of pad geometry, lead geometry, and local return-path structure in each layout. Those values are summarized later in Chapter 4 (Table 4.1) together with the corresponding circuit-validation results.

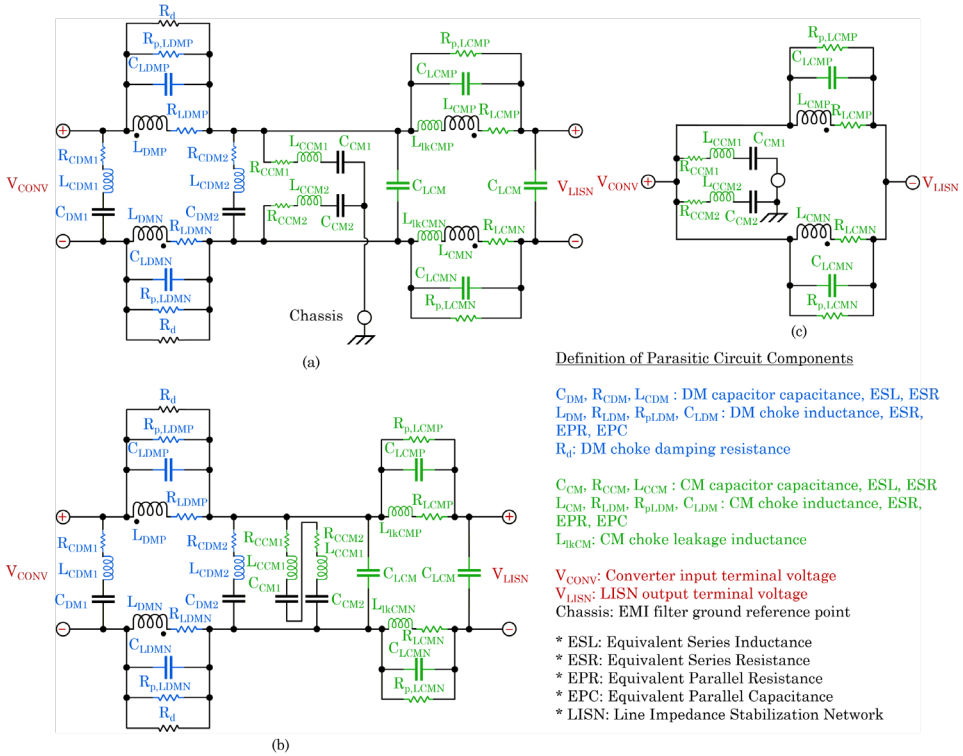


Figure 2.4: Full DM/CM parasitic circuit model used for circuit-level validation: (a) full parasitic EMI-filter circuit network including DM- and CM-stage parasitics, converter/LISN ports, and chassis reference; (b) DM-equivalent parasitic circuit used for differential-mode insertion-loss and output-impedance analysis; and (c) CM-equivalent parasitic circuit used for common-mode insertion-loss and output-impedance analysis.

Within Fig. 2.4, the symbols $C$, $L$, and $R$denote capacitance, inductance, and resistance terms, respectively, while $R_p$ denotes an equivalent parallel resistance branch. The subscripts DM and CM identify differential-mode and common-mode branches, $P$ and $N$ denote the positive-line and negative-line paths, and numeric suffixes distinguish different capacitors or branches of the same type. Thus, for example, $C_{DM1}$ and $C_{DM2}$ denote the two DM capacitors, $L_{CMP}$ and $L_{CMN}$ denote the two CM-choke windings, and $L_{lkCMP}$ and $L_{lkCMN}$ denote the associated leakage-inductance terms.

### 2.2.1 DM/CM Definitions, Insertion Loss, and Output Impedance

For a two-conductor line, differential-mode (DM) and common-mode (CM) voltages are defined from the conductor voltages $V_P$ and $V_N$ as

$$V_{DM} = V_P - V_N, V_{CM} = \frac{V_P + V_N}{2} \tag{2.15}$$

Similarly, the modal currents are defined as

$$I_{DM} = \frac{I_P - I_N}{2}, I_{CM} = I_P + I_N$$

with inverse relations

$$I_P = I_{DM} + \frac{I_{CM}}{2}, I_N = -I_{DM} + \frac{I_{CM}}{2}.$$

These definitions are used throughout the thesis to separate differential-mode (DM) and common-mode (CM) excitation/termination conditions for both measurement and modeling.

Insertion loss is reported as the transmission magnitude in decibels, so that stronger attenuation appears as a more negative value:

$$IL(f) = 20\log_{10} \left| \frac{\tilde{V}_{out}(f)}{\tilde{V}_{in}(f)} \right| \tag{2.16}$$

where $\tilde{V}_{in}$ and $\tilde{V}_{out}$ are the phasor input and output voltages under the specified DM or CM test condition.

For each mode, the output impedance is defined by injecting a small-signal test current at the output and measuring the resulting output voltage:

$$Z_{out}(f) = \frac{\tilde{V}_{test}(f)}{\tilde{I}_{test}(f)} \qquad (2.17)$$

When measured or simulated S-parameters are available, these quantities may also be obtained using standard two-port relations:

$$IL(f) = 20\log_{10} | S_{21}(f) |, Z_{out}(f) = Z_0 \frac{1 + S_{22}(f)}{1 - S_{22}(f)} \qquad (2.18)$$

where $Z_0$ is the reference impedance of the measurement system, typically $50\ \Omega$.

### 2.2.2 Incorporating the MoM Coupling Matrix into the Circuit Model

After extracting the loop-inductance matrix, the coupling between loop groups $i$and $j$may be expressed using the normalized coupling coefficient $k_{ij}$,

$$M_{ij} = k_{ij}\sqrt{L_{ii}L_{jj}} \qquad (2.19)$$

where $L_{ii}$ and $L_{jj}$ are the corresponding self-inductances and $M_{ij}$ is the mutual inductance between the two loops. This normalization provides an intuitive way to compare coupling strength across configurations.

Under magnetoquasistatic conditions and sinusoidal steady-state excitation, the inductive voltage associated with a coupled loop network can be written compactly as

$$\widetilde{\mathrm{V}}_L = j\omega \mathrm{L}\tilde{\mathrm{I}} \qquad (2.20)$$

where Lis the extracted loop-inductance matrix and Ĩis the loop-current phasor vector. In a SPICE-style implementation, the off-diagonal entries of Lcorrespond to mutual-inductance terms that couple the relevant branches of the filter model.

When the ratio between coupled loop currents is approximately fixed for the excitation under study, a mode-specific effective inductance seen by branch $i$can be approximated as

$$L_{i,\mathrm{eff}} = L_{ii} + \sum_{j \neq i} M_{ij} \frac{\tilde{I}_j}{\tilde{I}_i} \qquad (2.21)$$

This expression makes the sign dependence on current direction explicit and provides intuition for how placement-induced coupling changes can either raise or lower the observed equivalent series inductance.

This sign dependence is especially important for the common-mode choke. Under ideal CM excitation, the two windings carry in-phase currents, so the mutual term increases the net effective inductance. Under ideal DM excitation, the winding currents are anti-phase, so the mutual term reduces the net effective inductance. Similar coupling-driven shifts can also occur between the differential-mode chokes and nearby capacitor current loops,

thereby moving resonant peaks in insertion loss and output impedance and, in some layouts, increasing DM-to-CM mode conversion [4].

A two-winding common-mode choke can be represented using the inductance matrix

$$\begin{bmatrix} \tilde{V}_1 \\ \tilde{V}_2 \end{bmatrix} = j\omega \begin{bmatrix} L_{11} & M \\ M & L_{22} \end{bmatrix} \begin{bmatrix} \tilde{I}_1 \\ \tilde{I}_2 \end{bmatrix} \qquad (2.22)$$

For symmetric windings, $L_{11} = L_{22} = L$, and the effective inductances under ideal common-mode and differential-mode excitation become

$$L_{CM,CMC} = L + M, L_{DM,CMC} = L - M \qquad (2.23)$$

These relations explain why winding-to-winding coupling on the shared core can either increase the common-mode inductance or decrease the differential-mode inductance, depending on current direction.

The effective equivalent series inductances used to parameterize the capacitor branches in the DM/CM circuit model are not simply isolated part ESL values. In the assembled EMI filter, the voltage across a capacitor branch includes both its self-inductive drop and the induced voltage contributed by nearby current loops, including the common-mode choke windings and the differential-mode choke branches. The extracted PEEC/MoM self- and mutual-inductance terms therefore provide a compact means of capturing this interaction. The resulting configuration-specific effective ESL values are reported later in Chapter 4 (Table 4.1).

Figure 2.5 illustrates the two-loop interpretation used to convert the extracted inductance matrix into an equivalent capacitor-branch ESL. The primary loop represents the dominant choke current $i_{L1}(t)$, and the secondary loop represents the capacitor-branch

current $i_{L2}(t)$ flowing through an equivalent inductive branch $L_2$. The coupling between the two loops is represented by the mutual inductance $M$.

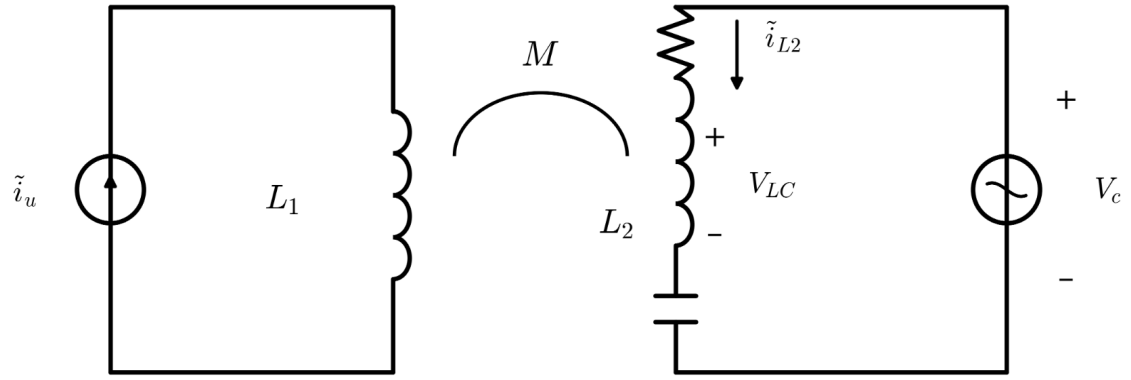


Figure 2.5. Coupled-loop model used to interpret extracted coupling terms and derive an equivalent ESL for capacitor branches.

Under the assumptions that *(i)* the dominant choke current waveform $i_{L1}(t)$ is only weakly perturbed by the coupling under study, and *(ii)* the capacitor terminal voltage may be treated as a prescribed excitation, the coupled-inductor relation for the secondary loop may be written as

$$v_{LC}(t) = M\frac{di_{L1}(t)}{dt} + L_2\frac{di_{L2}(t)}{dt} \qquad (2.24)$$

Solving for the induced current in the secondary loop gives

$$i_{L2}(t) = \frac{1}{L_2}\left[\int v_{LC}(t)\,dt - M\,i_{L1}(t)\right] \qquad (2.25)$$

In the full multi-loop network, the same idea generalizes naturally to an effective inductance seen by branch $i$, obtained by collecting all self- and mutual-inductive contributions into a single equivalent quantity:

$$L_{ESL,i}^{\text{eff}} = \frac{\tilde{V}_{L,i}}{j\omega\tilde{I}_i} = L_{ii} + \sum_{j\neq i} M_{ij}\frac{\tilde{I}_j}{\tilde{I}_i} \qquad (2.26)$$

The effective ESL values summarized in Chapter 4 (Table 4.1) were generated using this current-weighted reduction at the reference frequency of 1 MHz.

### 2.2.3 Practical Workflow Used in This Thesis and the Conference Study

The workflow used throughout this thesis follows four steps. First, a compact set of current loops is defined to represent the dominant EMI-relevant current paths of the filter assembly. Second, an $8 \times 8$loop-inductance matrix containing self and mutual terms is extracted using the reduced-order MoM kernel discretization, with ferrite effects incorporated through an effective permeability calibrated at 1 MHz. Third, the loop-level inductance matrix is mapped into the full DM/CM parasitic circuit model by assigning each loop to its associated ESL branch and inserting mutual couplings between the relevant branches. Fourth, both spatial metrics (near-field $H$-maps) and circuit metrics (insertion loss and output impedance) are evaluated, enabling rapid comparison across multiple hardware configurations. This emphasis on connecting physically extracted coupling parameters to both conducted and near-field EMI metrics is consistent with recent modal and coupled-circuit perspectives in the EMI literature [1], [2], [12].

### 2.2.4 Additional Governing Equations from the Literature

Several foundational relations are included here for completeness and to make explicit connections between the reduced-order filament model used in this thesis and the full PEEC / MoM formulations used in prior work. These equations also serve as a starting point for future work that adds capacitive (electric-field) extraction to the present inductive framework [5], [8].

Starting from Maxwell's equations in phasor form, the magneto-quasi-static (MQS) approximation assumes that wave propagation and displacement current effects are negligible at the dimensions and frequencies of interest (see [8], and the quasi-static discussion in [9]).

$$\begin{aligned} \nabla \times \mathrm{E} &= -\frac{\partial \mathrm{B}}{\partial t}, \\ \nabla \times \mathrm{H} &= \mathrm{J} + \frac{\partial \mathrm{D}}{\partial t}, \\ \nabla \cdot \mathrm{D} &= \rho_v, \\ \nabla \cdot \mathrm{B} &= 0 \end{aligned} \tag{2.27}$$

$$\begin{aligned} \mathrm{B} &= \mu \mathrm{H}, \\ \mathrm{D} &= \epsilon \mathrm{E}, \\ \mathrm{J} &= \sigma \mathrm{E} \end{aligned} \tag{2.28}$$

Under MQS for conductive structures, the displacement current term $j\omega D$ in (2.27) is typically neglected, and retardation is small when the following dimensionless criteria hold:

$$\begin{aligned} k_0 L_{\max} &\ll 1, \\ R &\ll \lambda, \\ \frac{\partial}{\partial t} &\rightarrow j\omega \end{aligned} \tag{2.29}$$

Traditional PEEC formulations compute not only partial inductances but also coefficients of potential (electric-field couplings). In a charge-based PEEC view, the coefficient-of-potential matrix $P$ relates surface charge on conductor panels to nodal potentials $V$ [5].

$$C = P^{-1}A^{-1}P \tag{2.30}$$

$$P = [p_1 \quad p_2 \quad \cdots \quad p_n], \qquad P^{-1} = \begin{bmatrix} q_1^T \\ q_2^T \\ \vdots \\ q_n^T \end{bmatrix} \tag{2.31}$$

When forming a compact reduced network, internal (unexcited) loop currents can be eliminated via Kron reduction / Schur complement. For the partition in (2.9), the reduced impedance seen by the known currents is [7], [3]:

$$i_1 = (Z_{11} - Z_{12}Z_{22}^{-1}Z_{21})^{-1}v_1 \tag{2.32}$$

Because the underlying magnetostatic kernels are reciprocal, the assembled impedance/inductance matrices should be symmetric (up to numerical error). A common stabilization is to explicitly enforce symmetry [5], [8]:

$$\begin{aligned} R_{ac} &= R_{dc}\left(\frac{x}{2}\right)\left(\frac{I_0(x)}{I_1(x)}\right), \\ x &= a\sqrt{\frac{\omega\mu\sigma}{2}} \end{aligned} \tag{2.33}$$

At MHz frequencies, conductor losses can be approximated by the skin-effect penetration depth δ, which can be used to form a first-order estimate of an effective AC cross-section and segment resistance [8].

$$\delta = \sqrt{\frac{2\rho}{\omega\mu}} = \sqrt{\frac{\rho}{\pi f\mu}} \tag{2.34}$$

$$\begin{aligned} \mathrm{S} &= \mathrm{P}^{-1}\mathrm{AP}, \\ \mathrm{A} &= \mathrm{PSP}^{-1} \end{aligned} \tag{2.35}$$

In filament / partial-inductance approaches, diagonal (self) terms can be approximated using closed-form expressions for long conductors. One commonly used approximation for a straight round wire of length ℓ and radius a (ℓ ≫ a) is [5], [8]:

$$C = \epsilon \frac{A}{d} \tag{2.36}$$

Magnetic moment analysis provides an alternative interpretation of choke radiation trends by approximating a winding as an equivalent magnetic dipole [12]. For $N$ turns carrying current $I$ with enclosed area $A$ and normal direction $\hat{n}$ :

$$C(r) = \frac{\hat{n} \cdot r}{4\pi r^3} \tag{2.37}$$

$$A(r) = \frac{\mu_0}{4\pi} \int \frac{I(s)}{\|r - \hat{r}\|} \, d\ell \tag{2.38}$$

For conducted EMI interpretation, terminal quantities are often transformed into differential-mode (DM) and common-mode (CM) variables using a linear change of coordinates [7], [2], [11]. Using the conventions in (2.15):

$$\begin{aligned} P &= \begin{bmatrix} 1/2 & 1/2 \\ 1 & -1 \end{bmatrix}, \\ P^{-1} &= \begin{bmatrix} 1 & 1/2 \\ 1 & -1/2 \end{bmatrix} \end{aligned} \tag{2.39}$$

Mixed-mode scattering parameters provide a standard framework for quantifying differential-mode (DM) to common-mode (CM) conversion in two-conductor networks, which is central to conducted EMI analyses [3]– [4]. Starting from the single-ended incident and reflected waves ($a_1$, $a_2$) and ($b_1$, $b_2$), the transformation to differential/common-mode waves is:

$$V_d = V_P^+ - V_P^- - (V_N^+ - V_N^-), \quad (2.40)$$
$$V_c = 1/2\,[(V_P^+ - V_P^-) + (V_N^+ - V_N^-)]$$

The corresponding mixed-mode S-parameter definition is:

$$\begin{bmatrix} b_d \\ b_c \end{bmatrix} = \begin{bmatrix} S_{dd} & S_{dc} \\ S_{cd} & S_{cc} \end{bmatrix} \begin{bmatrix} a_d \\ a_c \end{bmatrix} \quad (2.41)$$

In this representation, $S_{cd}$ (differential-to-common conversion) and $S_{dc}$ (common-to-differential conversion) directly quantify imbalance-driven mode conversion [3]– [4].

For inductive extraction methods such as PEEC and MoM, the loop flux linkage and stored magnetic energy provide useful physical checks on the assembled inductance matrix and its symmetry/passivity [8]– [9]. The flux-linkage vector is:

$$\mathrm{V} = \mathrm{SI} \quad (2.42)$$

and the corresponding stored magnetic energy is:

$$d\Phi_{12} = \mathrm{B}_2 \cdot d\mathrm{S}_1 \quad (2.43)$$

$$= \left(\frac{\mu}{4\pi}\right) \frac{(i_2\, d\ell_2 \times \mathrm{r}_{12}) \cdot d\mathrm{S}_1}{r_{12}^3}$$

Under full-wave PEEC formulations, retardation can be incorporated by replacing the static $1/R$ kernel with a frequency-dependent $e^{-j k_0 R} / R$ kernel [8]. For a filament pair, the retarded partial inductance can be written as

$$\mathrm{A}_n(\mathrm{r}_m) = \frac{\mu_0}{4\pi} \int_{\ell_n} \frac{I_n e^{-j k_0 R_{mn}}}{R_{mn}}\, d\ell_n \quad (2.44)$$

Under MQS conditions ($k_0 R \ll 1$), $e^{-j k_0 R} \approx 1$ and (2.44) reduces to the familiar Neumann integral form in (2.2), which is the basis for the static kernels used in this thesis.

Equations (2.30)– (2.31) highlight what is omitted in the present thesis (a full capacitive extraction and charge-based PEEC formulation), while (2.27)– (2.29) justify MQS operation and numerical stability controls for the reduced model. Equations (2.40)– (2.41) summarize mixed-mode S-parameter definitions used to quantify DM↔CM conversion, and (2.42)– (2.44) provide complementary energy and full-wave kernel relationships that motivate inductance-matrix symmetry/passivity and the MQS static-kernel approximation.

# CHAPTER 3

# EXPERIMENTAL SETUP

This chapter describes the experimental hardware, PCB layouts, excitation conditions, and near-field measurement procedure used to validate the proposed MoM-style coupling model. Four physical PCB configurations are evaluated using identical components but different choke placements and orientations, reflecting the layout-driven coupling effects emphasized in prior parasitic-coupling and choke-modeling studies [1], [5]. Two excitation cases are considered for each configuration: differential-mode (DM) excitation and common-mode (CM) excitation. These cases allow the model to be validated across different dominant current paths, mode-conversion tendencies, and magnetic near-field emission patterns [3], [4], [11].

## 3.1 EMI Filter Test PCB and Components

The experimental hardware is a $100$ mm $\times$ $100$ mmEMI filter PCB populated with one common-mode choke (CMC) and two differential-mode (DM) chokes, together with several film and ceramic capacitors that form localized current loops. The CMC is denoted $L_1$ and contains two windings, $L_{1P}$ and $L_{1N}$. The two DM chokes are denoted $L_2$ and $L_3$. Capacitors are denoted $C1_1$, $C4_1$, $C2$ , and $C3$, consistent with the component identifiers used on the PCB silkscreen and in the modeling codebase. The corresponding circuit schematic and PCB layout are shown in Figs. 3.1 and 3.2. Optional footprints $C1_2$

and $C4_2$ were included in the board design for flexibility, but these provisions were not populated in the present experiments.

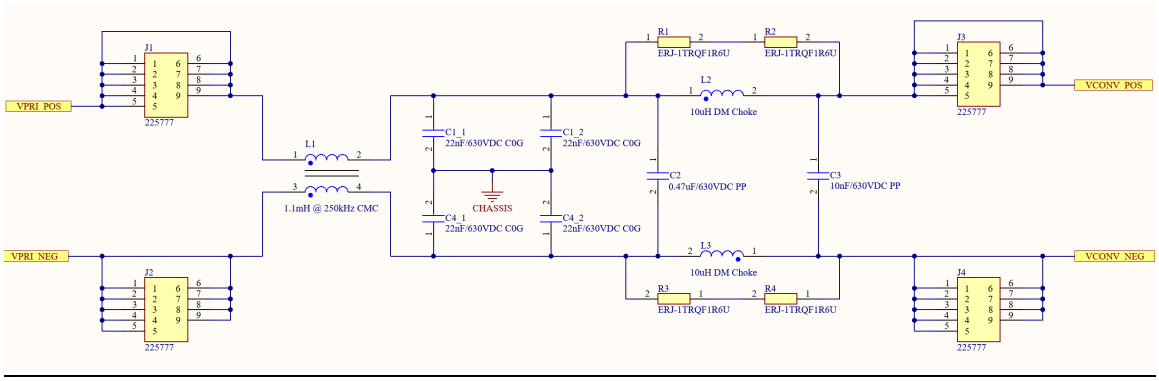


Figure 3.1: Altium schematic of the EMI filter test PCB used in this study. The design includes the common-mode choke $\boldsymbol{L_1}$, differential-mode chokes $\boldsymbol{L_2}$ and $\boldsymbol{L_3}$, and the capacitor network used to realize the DM and CM filtering paths. Optional provisions $\boldsymbol{C1\_2}$ and $\boldsymbol{C4\_2}$ are shown for completeness but were not populated for the present experiments.

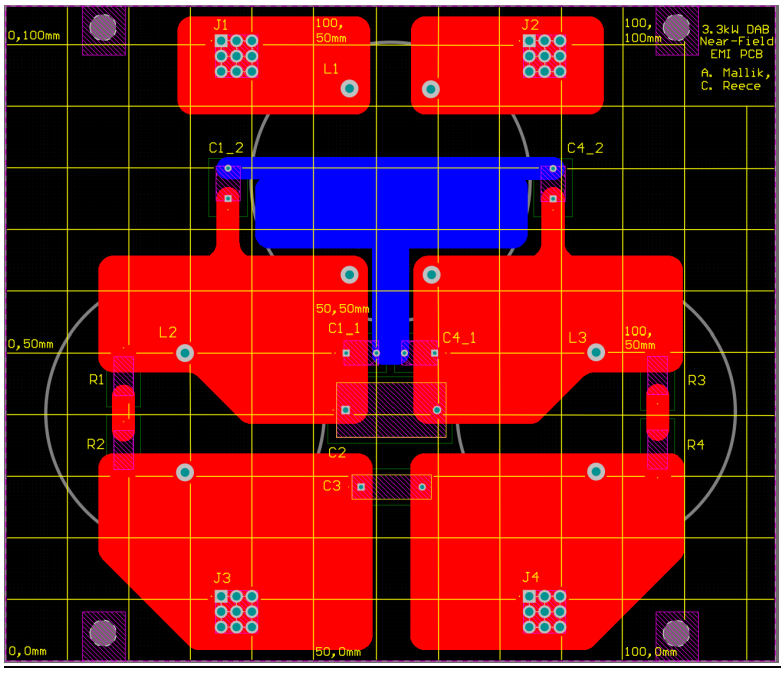


Figure 3.2. Altium PCB layout of the EMI filter hardware used in this study. The board dimensions are 100 mm × 100 mm, and the layout identifies the nominal locations of $L_1$, $L_2$, $L_3$, $C1\_1$, $C4\_1$, $C2$, and $C3$. Optional component sites $C1\_2$ and $C4\_2$ are shown but were not populated.

## 3.2 PCB Configurations

Four configurations ($C1$–$C4$) are studied. Each configuration uses the same components but changes the mounting orientation (flat versus on-edge) and the relative placement of the chokes. For model alignment, each configuration photograph was warped to a 100 mm × 100 mm reference frame, and the choke centroids were extracted to define loop centers. Choke orientations were then assigned using an in-plane or out-of-plane toroid-axis vector, depending on whether the core was mounted flat or on-edge. The assembled configurations used for photo-calibrated center and orientation extraction are shown in Fig. 3.3.

Configuration 1 places the common-mode choke $L_1$ on-edge near the top of the PCB, while the two differential-mode chokes $L_2$ and $L_3$ are mounted on-edge near the lower portion of the board. In the reduced-order model, $L_1$ is assigned one in-plane axis orientation and $L_2/L_3$ are assigned an orthogonal in-plane orientation to match the observed winding projection.

Configuration 2 mounts all chokes flat, so that the toroid axes are normal to the PCB plane. This configuration provides a baseline in which the dominant coupling differences arise primarily from planar separation rather than on-edge orientation.

Configuration 3 mounts all chokes on-edge with similar projected winding orientation in the $x$–$y$ plane. The common-mode choke remains near the top-center region of the PCB, with $L_2$ and $L_3$ positioned near the lower-left and lower-right regions, respectively.

Configuration 4 also mounts all chokes on-edge and with similar projected orientation, but places $L_2$ and $L_3$ more symmetrically near the lower corners of the PCB. This arrangement provides a useful comparison case for assessing how relative spacing and symmetry alter coupling trends.

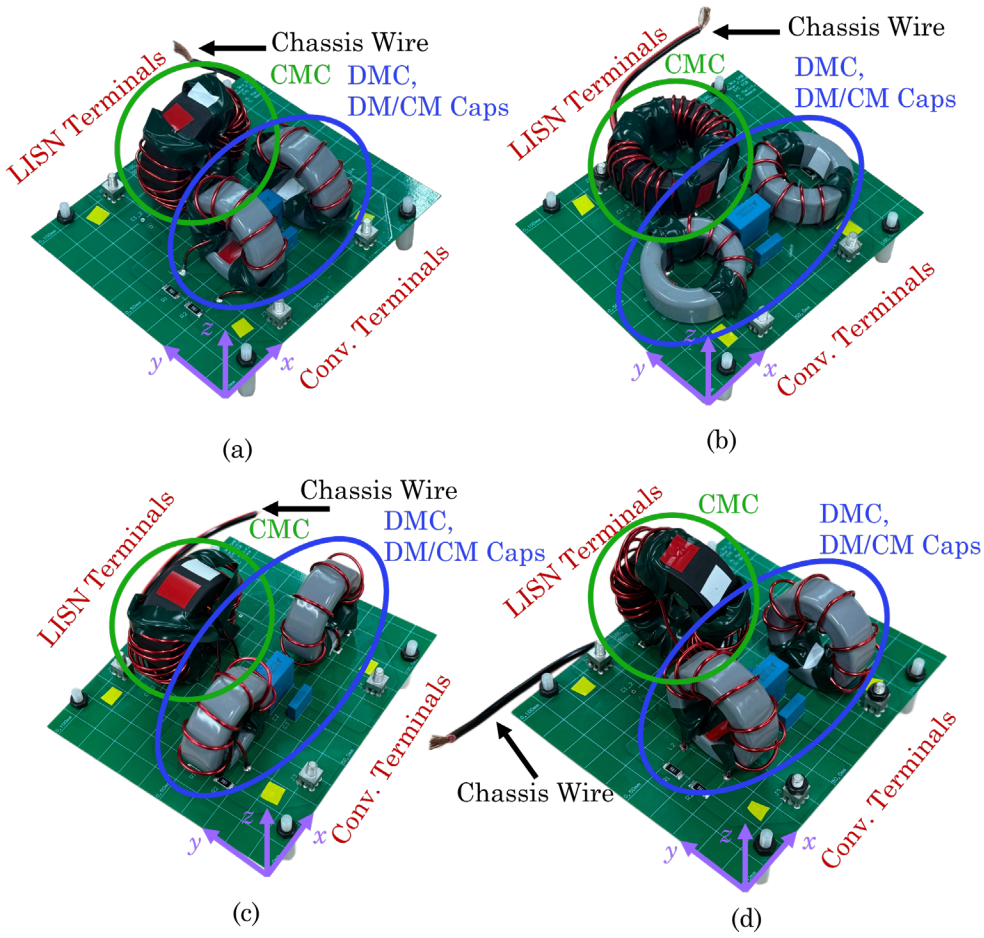


Figure 3.3: Photograph-based reference views of the four PCB configurations used for photo-calibrated center and orientation extraction: (a) Configuration 1, with the common-mode choke mounted on-edge near the LISN side and the differential-mode chokes mounted on-edge near the converter side; (b) Configuration 2, with all chokes mounted flat; (c) Configuration 3, with all chokes mounted on-edge and aligned similarly in the board plane; and

(d) Configuration 4, with all chokes mounted on-edge and the differential-mode chokes positioned more symmetrically near the lower board corners. In each panel, the green outline identifies the common-mode choke region, the blue outline identifies the differential-mode choke and capacitor region, the red labels indicate the LISN and converter terminals, and the $\boldsymbol{x}$–$\boldsymbol{y}$–$\boldsymbol{z}$ triad denotes the board-fixed coordinate system used for geometry calibration.

## 3.3 Excitation Cases and Current Phasors

For each configuration, two excitation cases are defined*: (i)* a DM excitation circuit, in which differential current flows primarily through the DM chokes, and *(ii)* a CM excitation circuit, in which common-mode current flows primarily through the CMC windings. These excitation scenarios were established using a 1 MHz LTSpice-equivalent filter model in which mutual coupling between the coils was initially neglected. Because the choke-current phasors are only weakly perturbed by mutual coupling at the operating frequency of interest, the uncoupled network solution provides a practical basis for specifying the source excitations used in the reduced-order model. This approach supports a clear initial separation between DM- and CM-dominated current paths before the full coupling matrix is introduced. Currents are reported as phasors at 1 MHz,

specified by magnitude in dB re 1A ($20\log_{10}(|I|/1\text{ A})$) and phase in degrees. In the model, $L_{DMP}$ and $L_{DMN}$ correspond to the two DM chokes ($L_2$ and $L_3$), while $L_{CMP}$ and $L_{CMN}$ correspond to the two common-mode choke windings ($L_{1P}$ and $L_{1N}$).

Table 3.1: Excitation current phasors at **1** MHz used for the DM and CM excitation cases in Configurations 1–4.

| **Configuration** | **Excitation** | ***L₂ (L_DMP)*** | ***L₃ (L_DMN)*** | ***L_1P (L_CMP)*** | ***L_1N (L_CMN)*** |
|---|---|---|---|---|---|
| 1 | DM | -66.140 dB, -11.444° | -65.780 dB, -5.979° | -94.000 dB, 141.980° | -94.210 dB, -37.050° |
| 1 | CM | -102.396 dB, -56.842° | -102.372 dB, 128.026° | -73.899 dB, 1.358° | -73.659 dB, 1.380° |
| 2 | DM | -65.700 dB, -10.944° | -65.640 dB, -5.742° | -93.940 dB, 142.180° | -93.960 dB, -37.690° |
| 2 | CM | -103.168 dB, -54.109° | -102.601 dB, 130.045° | -74.595 dB, 1.198° | -74.512 dB, 1.305° |
| 3 | DM | -63.216 dB, 12.650° | -63.160 dB, 16.483° | -91.440 dB, -177.035° | -91.440 dB, 2.970° |

| Configuration | Excitation | $L_2$ ($L_{DMP}$) | $L_3$ ($L_{DMN}$) | $L_{1P}$ ($L_{CMP}$) | $L_{1N}$ ($L_{CMN}$) |
|---|---|---|---|---|---|
| 3 | CM | -100.255 dB, -41.870° | -100.127 dB, 142.861° | -73.773 dB, 26.310° | -73.488 dB, 26.357° |
| 4 | DM | -62.696 dB, 12.397° | -62.548 dB, 15.988° | -120.969 dB, -79.287° | -120.962 dB, 100.600° |
| 4 | CM | -101.098 dB, -37.680° | -100.810 dB, 146.521° | -60.933 dB, 51.424° | -64.755 dB, -112.800° |

## 3.4 Near-Field Measurement Setup and Procedure

### 3.4.1 Instrumentation and Scan Grid Definition

Near-field magnetic scanning was performed using a Tektronix H10 H-field loop probe connected to a Rohde & Schwarz spectrum analyzer. When additional sensitivity was required in low-signal regions, an external preamplifier was inserted between the probe and the analyzer. The probe was translated over the PCB on a uniform $x$–$y$ grid with a 10 mm pitch, yielding a spatial map of the measured probe response. The nominal scan window covered an 80 mm × 90 mm region containing the choke and capacitor network so that both the filter region and adjacent edge effects were captured.

The PEEC/MoM post-processing produces field maps on the full 100 mm × 100 mm PCB coordinate system, whereas some processed measurement figures are cropped to a smaller window centered on the filter region for improved visual focus.

Accordingly, measured and modeled maps were compared only after cropping or resampling to a common coordinate extent and axis scale so that component footprints and high-field regions were not visually distorted by mismatched plotting windows.

To provide repeatable excitation across configurations, the filter input was driven by a sinusoidal source at $f = 1$ MHz with $V_{\mathrm{RMS}} = 0.7071$ V. Differential-mode (DM) excitation was applied as equal-magnitude, 180°out-of-phase drive on the DC+ and DC− conductors, whereas common-mode (CM) excitation was applied as in-phase drive relative to chassis/ground, following the phasor conventions summarized in Table 3.1. For both excitation cases, a $50\ \Omega$ termination was used to approximate a well-defined load and to maintain compatibility with the insertion-loss and impedance measurements described below.

In addition to spatial field scans, circuit-level characterization was performed using an OMICRON Bode 100 vector network analyzer (VNA). Mode-specific insertion loss and output impedance were measured with a standardized $50\ \Omega$ source impedance and $50\ \Omega$ termination to enable direct comparison with the reduced-order circuit model of Section 2.2. These measurements provide an independent validation channel: if the extracted coupling matrix is physically consistent, then the same parameters that improve agreement in the near field should also shift the predicted resonant features in insertion loss and output impedance toward the measured responses.

The primary validation planes are $z = 13$ mm and $z = 35$ mm, with intermediate scans at $z = 14$–$18$ mm used to assess sensitivity to probe height and to align the model with the realized probe placement. For each configuration, separate scans were acquired for DM

and CM excitation. Near-field scanning has been used in prior work to assess and reduce magnetic emissions from inductors and power-electronic subsystems, including toroidal structures [11], [12].

If the measured quantity is reported as probe output, the analyzer reading is expressed as

$$V_{\mathrm{dB}\mu\mathrm{V}} = 20\log_{10}\left(\frac{V_{\mathrm{RMS}}}{1\ \mu\mathrm{V}}\right)$$

If an external preamplifier with gain $G_{\mathrm{amp}}(f)$ is used, the voltage referred back to the probe port is

$$V_{\mathrm{probe,dB}\mu\mathrm{V}} = V_{\mathrm{SA,dB}\mu\mathrm{V}} - G_{\mathrm{amp}}(f)$$

For a $50\ \Omega$ analyzer input, the corresponding probe output power is

$$P_{\mathrm{probe,dBm}} = V_{\mathrm{probe,dB}\mu\mathrm{V}} - 107$$

When absolute field-strength conversion is required, the magnetic flux density is obtained from the published H10 transfer relation,

$$B = 10^{\frac{P_{\mathrm{probe,dBm}} - S_{H10} - 20\log_{10}(f_{\mathrm{MHz}})}{20}}, S_{H10} = 62$$

where $B$ is in tesla, $f_{\mathrm{MHz}}$ is the measurement frequency in megahertz, and $P_{\mathrm{probe,dBm}}$ is the probe output power in dBm. The corresponding magnetic-field magnitude is then

$$H = \frac{B}{\mu_0}$$

If the results are presented only as measured probe response rather than calibrated field strength, then the data should remain in $V_{\mathrm{dB}\mu\mathrm{V}}$, and the $B$-to-$H$ conversion should be omitted.

A key step in the modeling workflow is mapping physical hardware to model geometry and material parameters. Choke center locations and in-plane orientations are obtained from photo calibration, as described in Section 3.2. For the ferrite cores, a single effective permeability is calibrated at 1 MHz so that the modeled self-inductance matches measured or datasheet inductance targets. This effective-parameter approach is consistent with common modeling strategies for EMI filtering chokes [5]. The common-mode choke is modeled as two explicit windings, $L_{1P}$ and $L_{1N}$, on the same core, separated by a small offset comparable to the wire diameter to avoid coincident segments while preserving strong mutual coupling through the shared core.

Capacitor loops are modeled geometrically using the pad-to-pad spacing on the PCB together with an effective vertical loop height. This height represents the current path rising from one pad through the component body and returning to the other pad. While simplified, this representation captures the dominant inductive coupling between the chokes and the capacitor return loops that contributes to layout-dependent parasitic interaction in EMI filters [1].

# CHAPTER 4

# RESULTS AND DISCUSSION

This chapter presents the coupling-matrix and near-field results obtained from the proposed model for the four PCB configurations. Results are discussed for both differential-mode (DM) and common-mode (CM) excitation cases, and the impact of choke placement and orientation on coupling and field distribution is interpreted using quasi-static magnetic-field intuition and layout-driven coupling concepts reported in prior EMI-filter studies [1], [5], [7]. Where available, simulated field maps are compared qualitatively against measured probe scans and against published near-field behavior for toroidal inductors [11], [12].

## 4.1 Extracted Coupling Matrices

To compare coupling strength across loop pairs, the normalized coupling coefficient is computed from the extracted mutual and self-inductance terms as

$$k_{ij} = \frac{M_{ij}}{\sqrt{L_{ii}L_{jj}}} \qquad (4.1)$$

where $M_{ij}$is the mutual inductance between loops $i$and $j$, and $L_{ii}$and $L_{jj}$are the corresponding self-inductances. The coupling coefficient provides a dimensionless measure of interaction strength and allows mutual-coupling trends to be compared consistently across configurations.

Because the inductors are identical across configurations and the model preserves the same winding geometry, the self-inductances of $L_{1P}$, $L_{1N}$, $L_2$, and $L_3$ remain approximately constant. In contrast, the mutual-inductance terms—and therefore the normalized coupling coefficients—vary with relative separation and orientation. As a result, configuration-dependent trends are expected primarily in the off-diagonal terms of the extracted matrix.

Table 4.1 summarizes the configuration-specific effective equivalent series inductance (ESL) values used in the circuit-level model. Because these values are derived from the extracted loop-inductance matrix, they reflect not only the nominal capacitor parasitics but also layout-dependent inductive interaction between capacitor branches and nearby choke loops.

To support design intuition and committee review, Tables 4.2–4.5 list the extracted mutual-inductance terms between the four capacitor loops ($C_{DM1}$, $C_{DM2}$, $C_{CM1}$, and $C_{CM2}$) and the inductor/choke loops ($L_{DMP}$, $L_{DMN}$, $L_{CMP}$, and $L_{CMN}$) for each layout configuration at 1 MHz. In this notation, $L_{DMP} \equiv L_2$ and $L_{DMN} \equiv L_3$ denote the two differential-mode chokes; $L_{CMP} \equiv L_{1P}$ and $L_{CMN} \equiv L_{1N}$ denote the two common-mode choke windings; $C_{DM1} \equiv C1_1$ and $C_{DM2} \equiv C4_1$ denote the two differential-mode capacitor loops; and $C_{CM1} \equiv C2$ and $C_{CM2} \equiv C3$ denote the two common-mode capacitor loops. Values are reported in nH and preserve the sign convention implied by the PEEC/MoM loop orientation. Only the requested subset of terms is shown in the main text; the full symmetric matrix is available from the solver output.

Across configurations, the largest $|M_{ij}|$ terms typically occur between the capacitor loops and the physically nearest choke winding(s), which is consistent with dominant near-field magnetic coupling through local loop area and proximity. Sign changes indicate reversals in effective coupling polarity caused by loop orientation and return-path geometry, and these signs are important when incorporating mutual terms into the reduced-order circuit model.

Table 4.1. Configuration-specific effective equivalent series inductance (ESL) values used in the circuit-level model at 1 MHz.

| Capacitor | Reference ESL | Configuration 1 | Configuration 2 | Configuration 3 | Configuration 4 |
|---|---|---|---|---|---|
| CDM1 | 27.040 nH | 27.070 nH | 27.050 nH | 27.020 nH | 27.140 nH |
| CDM2 | 22.540 nH | 32.680 nH | 20.330 nH | 24.000 nH | 24.350 nH |
| CCM1 | 13.860 nH | 9.890 nH | 10.330 nH | 13.700 nH | 6.380 nH |
| CCM2 | 13.860 nH | 18.230 nH | 30.370 nH | 4.740 nH | 57.920 nH |

Table 4.2. Mutual inductance values $M_{ij}$ (nH) for Configuration 1 at 1 MHz.

| LDMP | LDMN | LCMP | LCMN | CDM1 | CDM2 | CCM |
|---|---|---|---|---|---|---|

| | | | | | | | |
|---|---|---|---|---|---|---|---|
| **CDM1** | 0.864nH | 0.679nH | 7.990nH | 7.220nH | — | -0.474nH | 0.112nH |
| **CDM2** | 0.569nH | 0.143nH | 0.311nH | -0.010nH | -0.474nH | — | 0.115nH |
| **CCM1** | 3.260nH | 3.380nH | 6.480nH | 5.780nH | 0.891nH | 0.925nH | 1.240nH |
| **CCM2** | 1.780nH | 6.060nH | 2.060nH | 1.930nH | 0.112nH | 0.115nH | — |

Table 4.3. Mutual inductance values $\boldsymbol{M_{ij}}$(nH) for Configuration 2 at 1 MHz.

| **LDMP** | **LDMN** | **LCMP** | **LCMN** | **CDM1** | **CDM2** | **CCM2** | |
|---|---|---|---|---|---|---|---|
| **CDM1** | -0.059nH | 0.958nH | 0.210nH | 0.219nH | — | -0.474nH | 0.112nH |
| **CDM2** | -0.022nH | 1.050nH | 0.136nH | 0.146nH | -0.474nH | — | 0.115nH |
| **CCM1** | -0.060nH | 0.356nH | 0.254nH | 0.264nH | 0.891nH | 0.925nH | 1.240nH |
| **CCM2** | 0.043nH | -2.210nH | 0.072nH | 0.074nH | 0.112nH | 0.115nH | — |

Table 4.4. Mutual inductance values $\boldsymbol{M_{ij}}$(nH) for Configuration 3 at 1 MHz.

| LDMP | LDMN | LCMP | LCMN | CDM1 | CDM2 | CCM2 | |
|---|---|---|---|---|---|---|---|
| **CDM1** | -0.368nH | 0.242nH | 2.570nH | 2.370nH | — | -0.474nH | 0.112nH |
| **CDM2** | -0.251nH | -4.120nH | 1.070nH | 0.904nH | -0.474nH | — | 0.115nH |
| **CCM1** | -1.600nH | -4.040nH | 3.210nH | 2.990nH | 0.891nH | 0.925nH | 1.240nH |
| **CCM2** | -1.000nH | 1.670nH | 1.140nH | 1.090nH | 0.112nH | 0.115nH | — |

Table 4.5. Mutual inductance values $\boldsymbol{M_{ij}}$(nH) for Configuration 4 at 1 MHz.

| LDMP | LDMN | LCMP | LCMN | CDM1 | CDM2 | CCM2 | |
|---|---|---|---|---|---|---|---|
| **CDM1** | 0.764nH | 2.090nH | -1.930nH | -1.720nH | — | -0.474nH | 0.112nH |
| **CDM2** | 0.382nH | 1.510nH | -3.010nH | -2.610nH | -0.474nH | — | 0.115nH |
| **CCM1** | 1.230nH | 16.700nH | -3.100nH | -2.760nH | 0.891nH | 0.925nH | 1.240nH |
| **CCM2** | -0.216nH | 1.660nH | -0.759nH | -0.691nH | 0.112nH | 0.115nH | — |

Across configurations, the largest $|M|$ terms typically occur between the capacitor loops and the physically closest choke winding(s), which aligns with dominant near-field magnetic coupling through the local loop area and proximity. Observed sign changes indicate a reversal in the effective coupling polarity caused by loop orientation and return-path geometry; these signs are essential when incorporating mutual terms into the reduced-order circuit model.

## 4.2 Coupling Trends Across Configurations

The strongest mutual coupling in the system occurs between the two windings of the common-mode choke, $L_{1P}$ and $L_{1N}$, because they share the same ferrite core. Coupling between the differential-mode chokes, $L_2$ and $L_3$, depends strongly on their spacing and on whether their effective magnetic dipole moments reinforce or oppose one another. Magnetic coupling among filter chokes has been identified as a contributor to conducted-EMI variation in wide-bandgap converter systems [5], [7]. Coupling between the chokes and capacitor loops is generally smaller, but these interactions can still influence near-field distributions because capacitor loops provide return paths that shape current flow at 1 MHz and can participate in CM-DM mode conversion when the structure is imbalanced [3], [4].

Across Configurations 1–4, the primary geometric factors are *(i)* whether the chokes are mounted flat or on-edge, which rotates the dominant magnetic-flux direction, and *(ii)* the relative alignment of the toroid axes. Configurations with on-edge mounting tend to produce more directional and localized field lobes in the scan plane, whereas flat mounting produces more symmetric patterns centered on each core. These trends are consistent with the magnetic-dipole interpretation of a current loop and with near-field emission patterns reported for toroidal inductors under orientation changes [11], [12].

## 4.3 Near-Field H-Map Results

Near-field maps were generated at multiple heights above the PCB for both DM and CM excitations. The field is calculated using the finite straight-segment Biot-Savart relation

summed over all discretized segments. Maps are reported as $|\ H\ |$ magnitude together with quiver plots indicating the in-plane direction of Re$\{H_{xy}\}$. These visualizations provide direct insight into how each configuration concentrates or disperses magnetic-field intensity across the PCB area, which is a common diagnostic in near-field emission studies of inductors and power-electronic assemblies [11], [12].

Configuration 3 is introduced first as a representative example because it exhibits clearly separated DM- and CM-dominated field regions at both near and higher observation planes. Figure 4.1 shows the simulated $|\ H\ |$ magnitude and in-plane direction maps for Configuration 3 under DM and CM excitation at $z = 13$ mm and $z = 35$ mm.

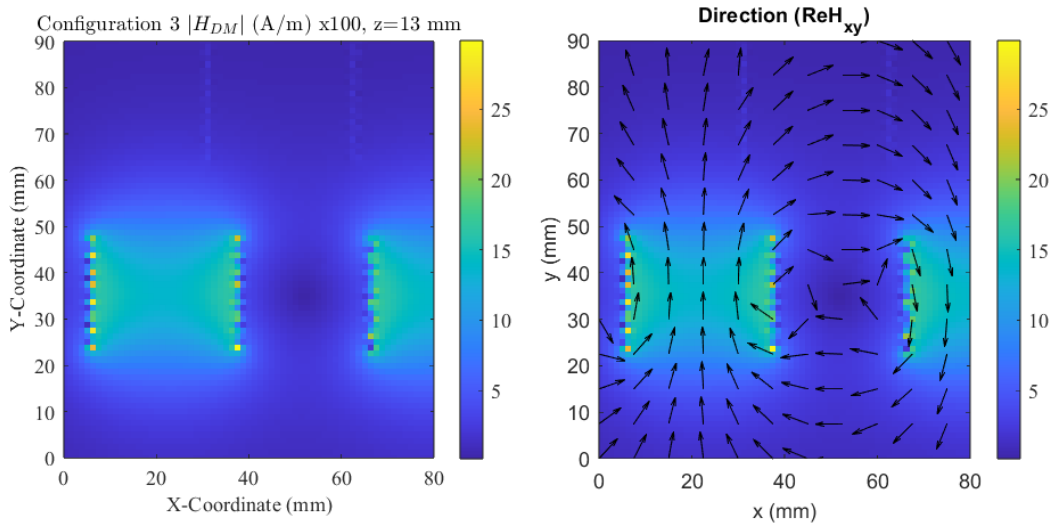


Figure 4.1. Example simulated H-field magnitude and in-plane direction maps for Configuration 3 under DM and CM excitation at $z = 13$ mm and $z = 35$ mm (100 × visualization scaling).

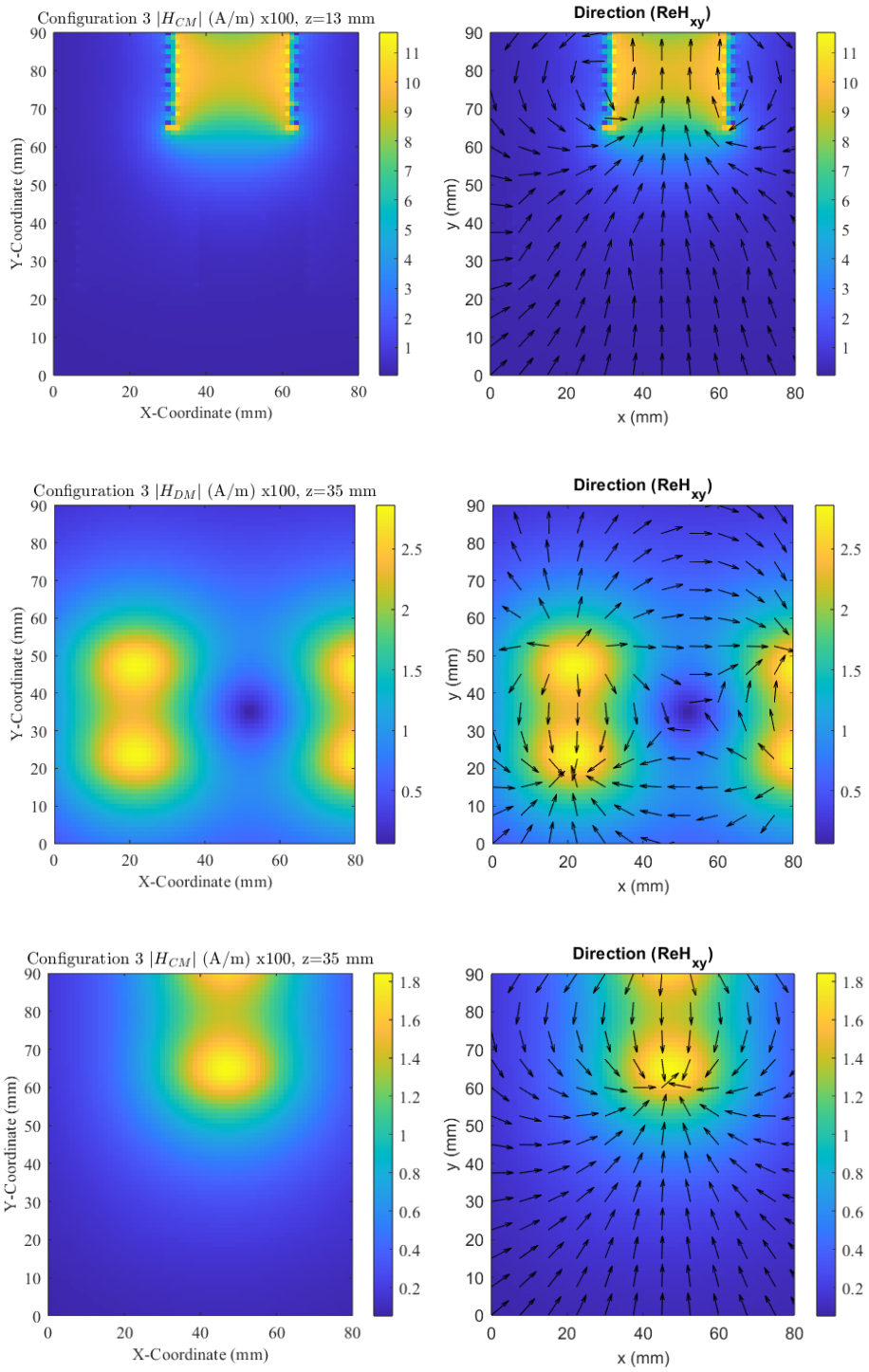


Figure 4.1. Example simulated H-field magnitude and in-plane direction maps for Configuration 3 under DM and CM excitation at $z = 13$ mm and $z = 35$ mm (100 × visualization scaling).

A short height sweep was also performed for Configuration 3 over $z = 13$–$18$ mm, together with a $z = 35$ mm reference plane. Figure 4.2 summarizes the DM and CM near-field maps as a function of observation height.

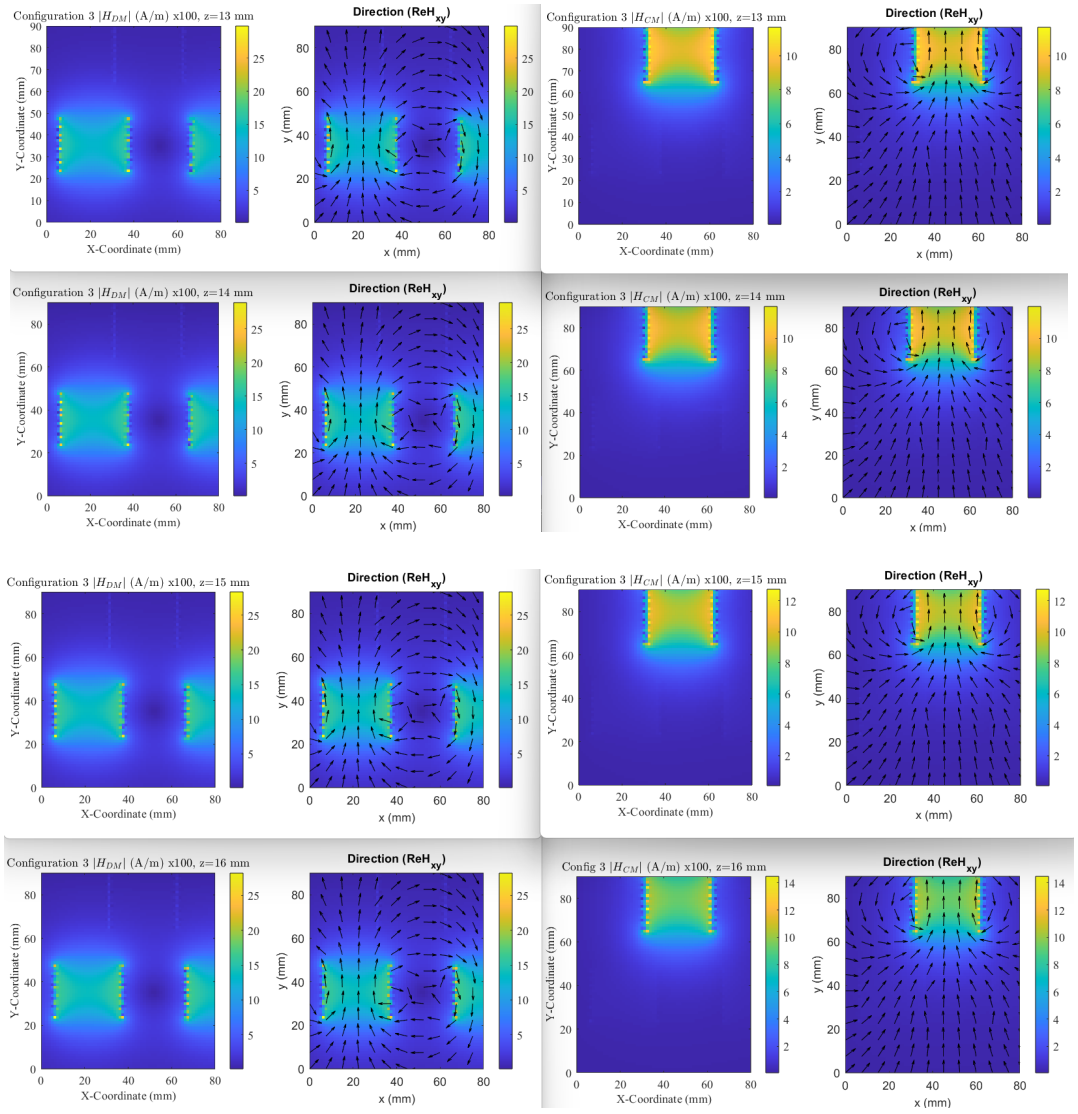


Figure 4.2. Height sweep for Configuration 3 ($z = 13$–$18$ mm and $z = 35$ mm) illustrating the dependence of DM/CM near-field magnitude and direction on probe height.

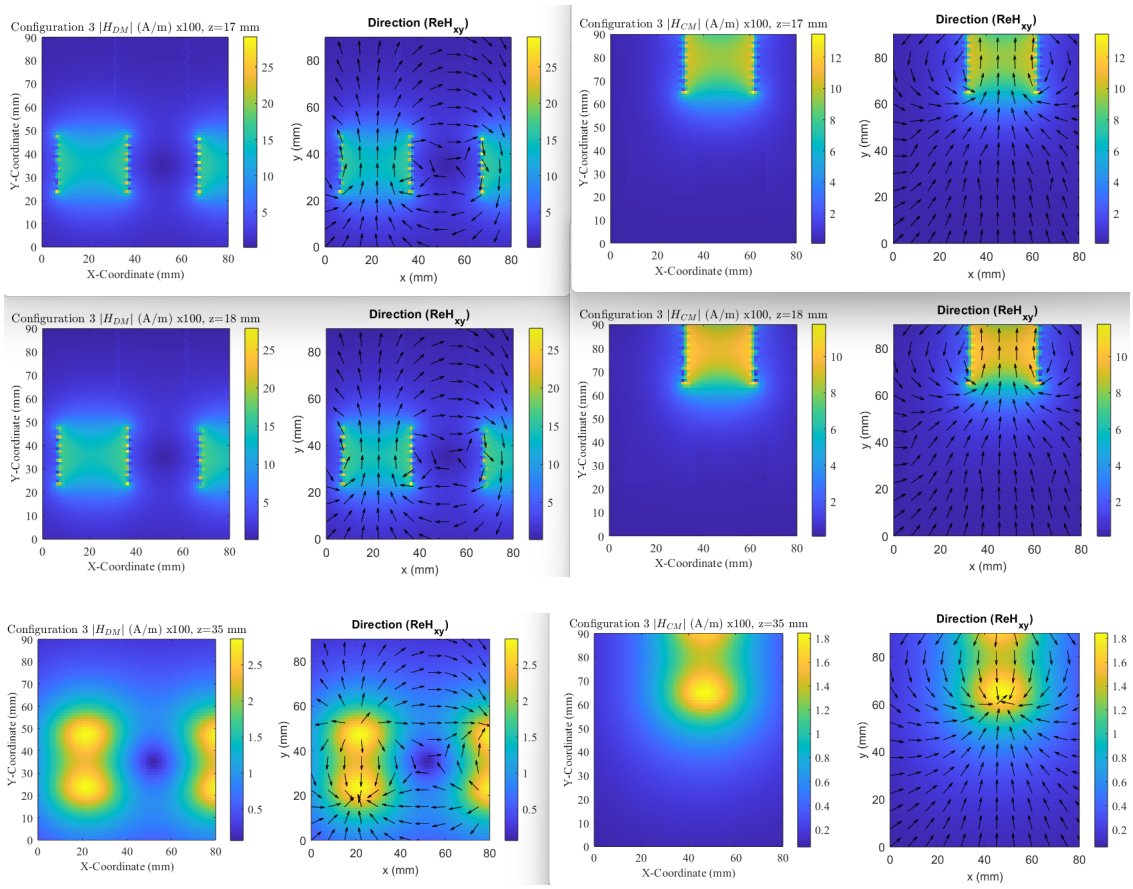


Figure 4.2. Height sweep for Configuration 3 ($z = 13$–$18$ mm and $z = 35$ mm) illustrating the dependence of DM/CM near-field magnitude and direction on probe height.

In addition to the representative Configuration 3 sweep, the same height-dependent analysis was performed for the remaining hardware layouts. Figure 4.3 summarizes the DM and CM excitation cases for Configuration 4 over $z = 13$–$18$ mm and $z = 35$ mm.

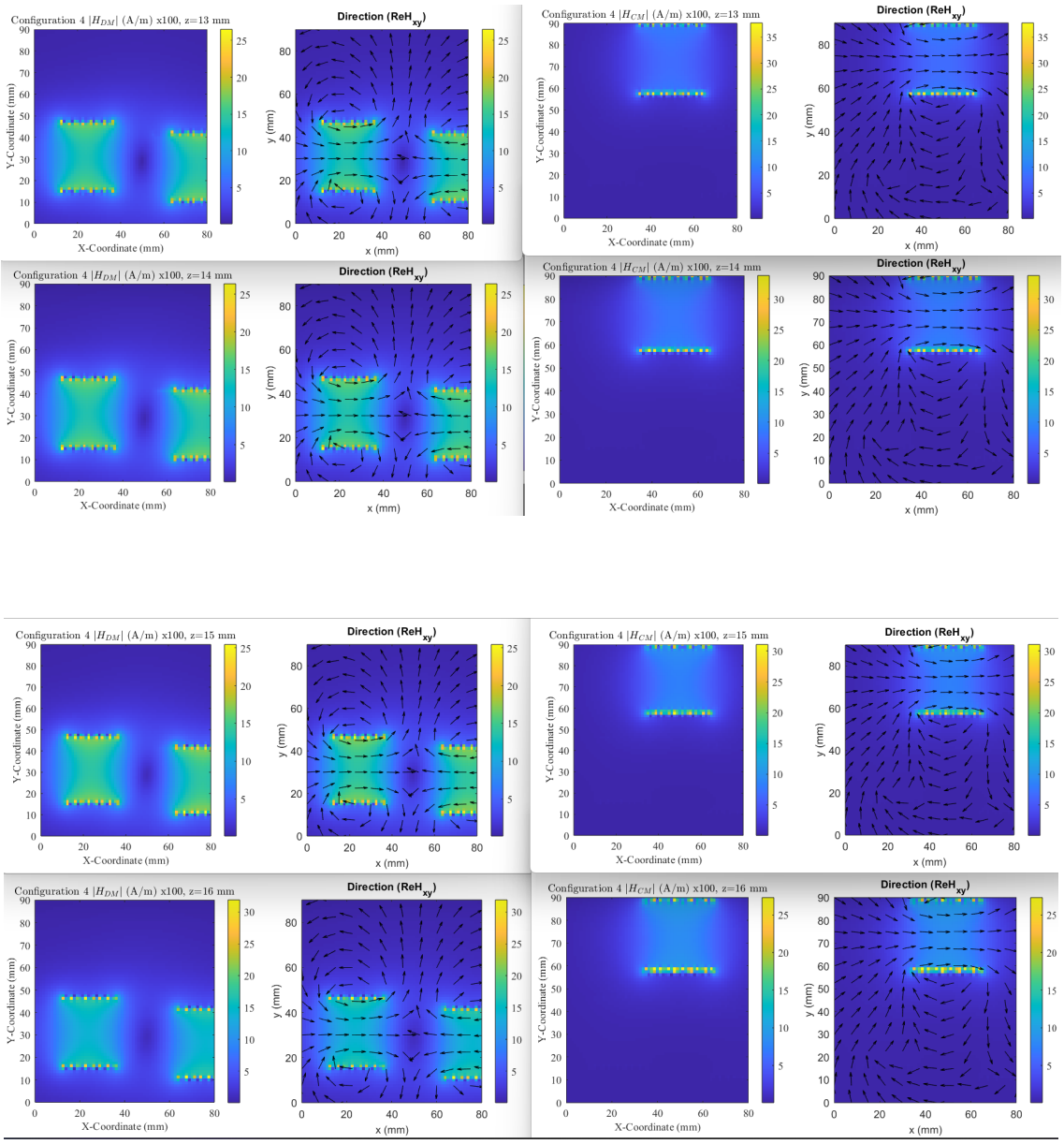


Figure 4.3. Configuration 4 simulated | $H$ | magnitude and in-plane direction maps for DM excitation (left pair in each row) and CM excitation (right pair in each row) across probe heights $z = 13$–$18$ mm and $z = 35$ mm (100 × visualization scaling).

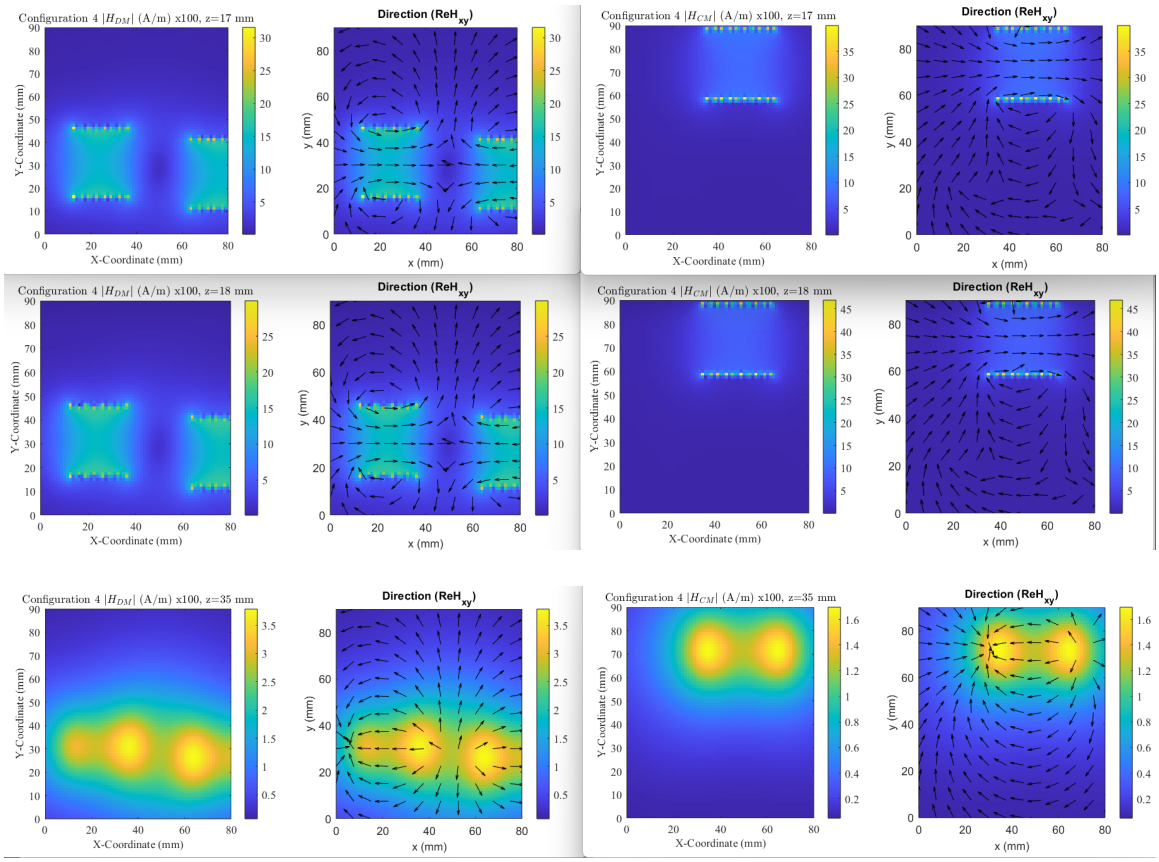


Figure 4.3. Configuration 4 simulated | $H$ | magnitude and in-plane direction maps for DM excitation (left pair in each row) and CM excitation (right pair in each row) across probe heights $z = 13$–$18$ mm and $z = 35$ mm (100 × visualization scaling).

Near-field results are shown in Figure 4.4, where the simulated magnetic-field magnitude and in-plane direction are swept from $z$ = 13 mm to $z$ = 18 mm and compared to a far-plane reference at $z$ = 35 mm. The dominant fields remain localized near the toroidal chokes, but the apparent spatial extent and peak magnitude change with probe height due to geometric spreading and reduced near-field coupling at larger $z$.

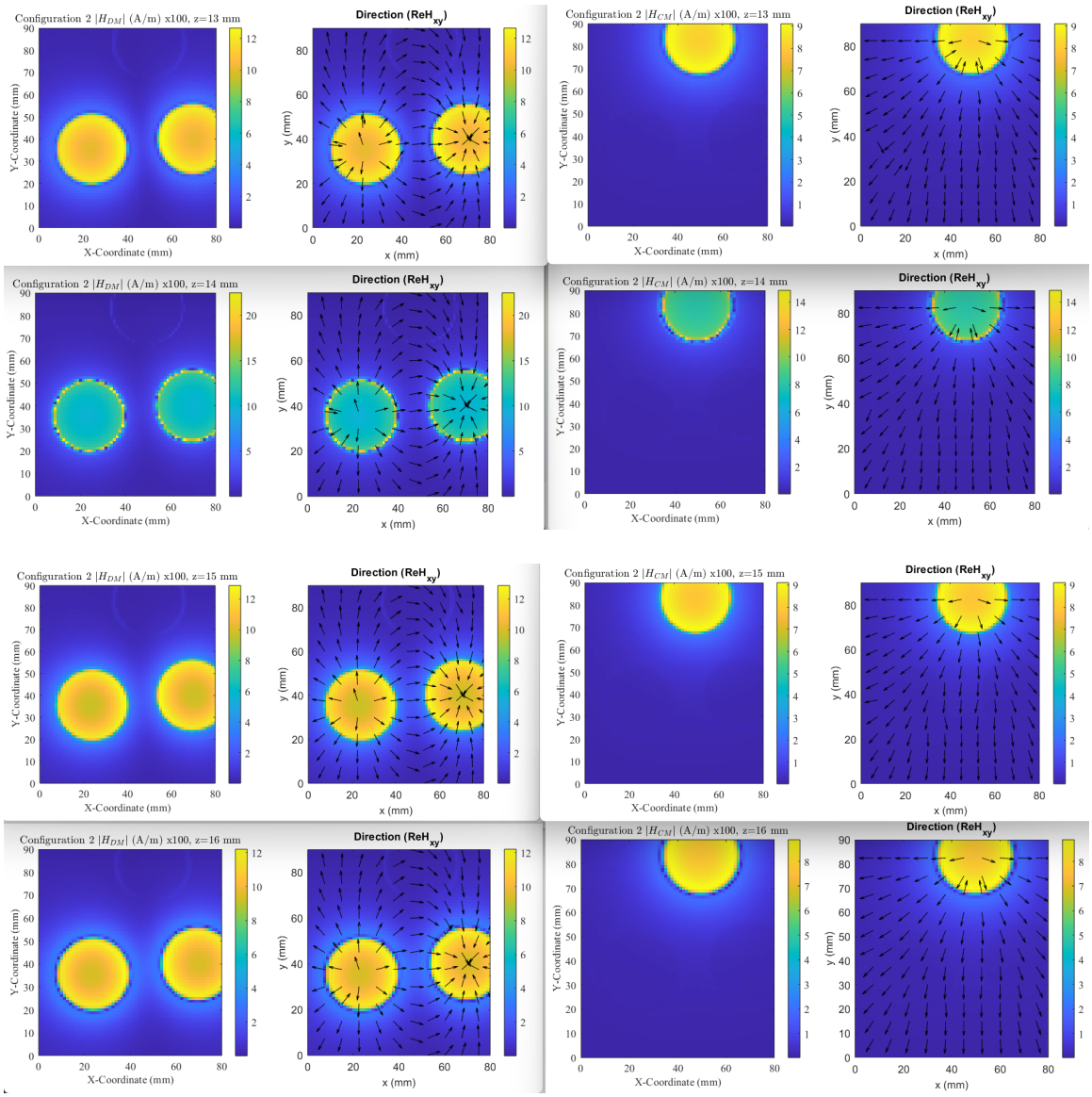


Figure 4.4. Configuration 2 simulated | $H$ | magnitude and in-plane direction maps for DM excitation (left pair in each row) and CM excitation (right pair in each row) across probe heights $z = 13$–$18$ mm and $z = 35$ mm (100 × visualization scaling).

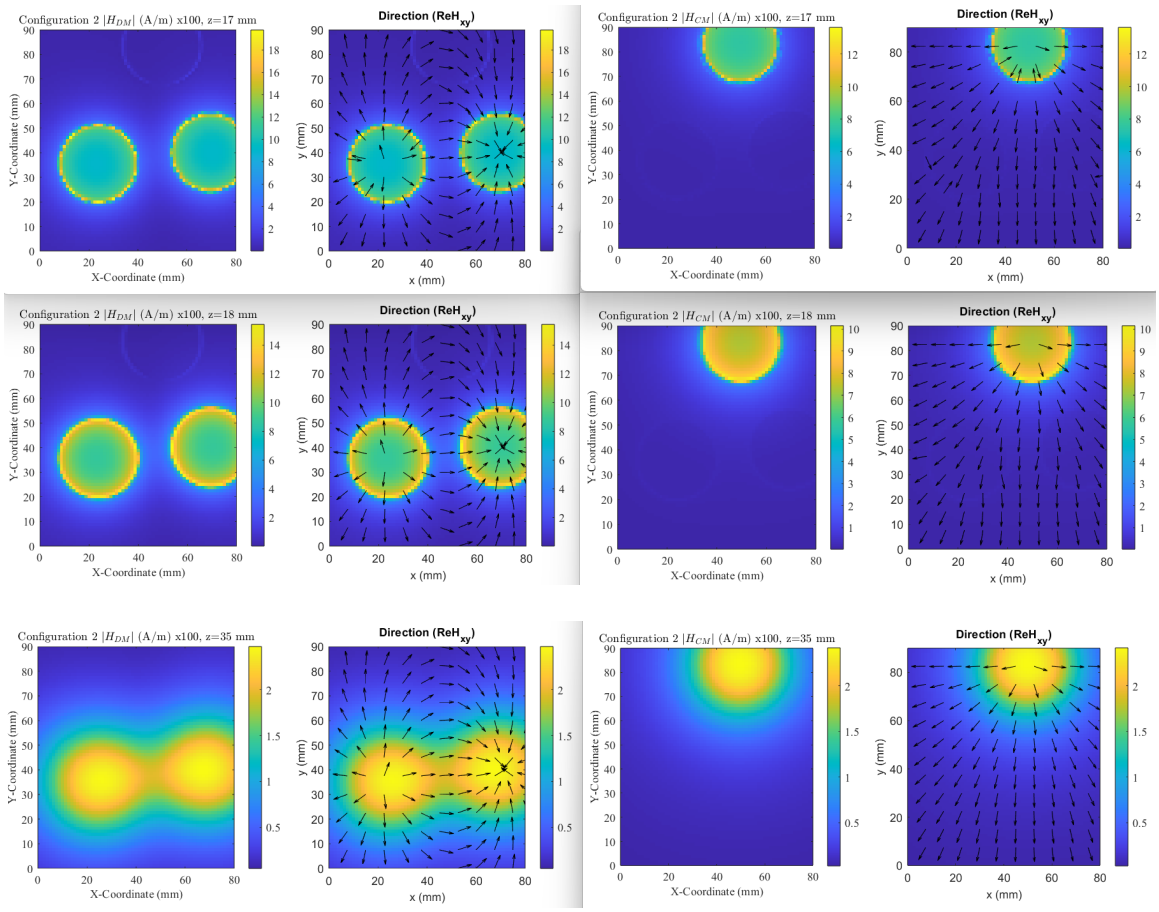


Figure 4.4. Configuration 2 simulated | $H$ | magnitude and in-plane direction maps for DM excitation (left pair in each row) and CM excitation (right pair in each row) across probe heights $z = 13$–$18$ mm and $z = 35$ mm (100 × visualization scaling).

Configuration 1 provides a baseline for how DM and CM magnetic fields localize around the inductors and common-mode choke as the probe height is reduced. Figure 4.5 summarizes the simulated DM and CM near-field maps for $z = 13$–$18$ mm and $z = 35$ mm.

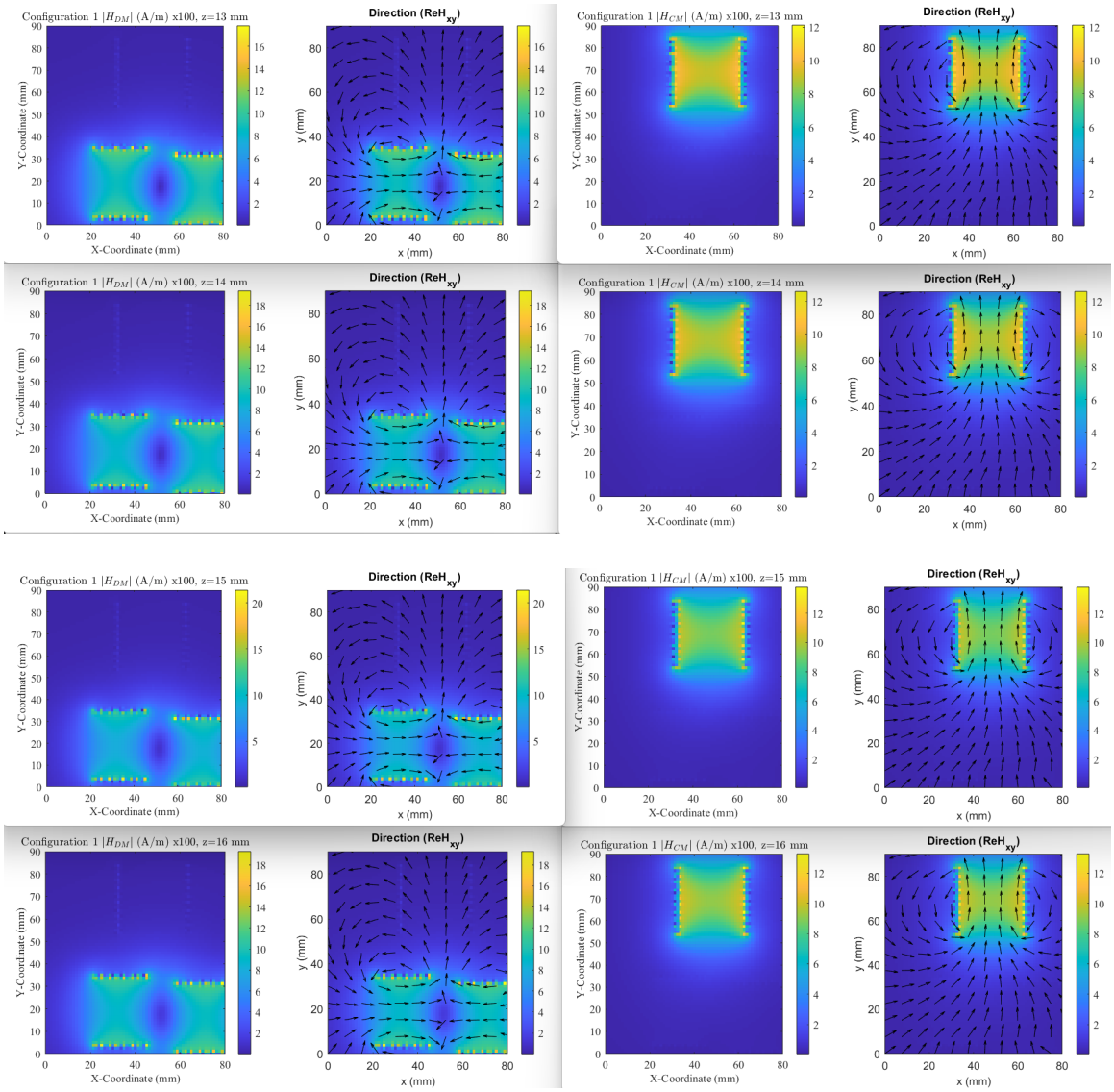


Figure 4.5. Configuration 1 simulated | $H$ | magnitude and in-plane direction maps for DM excitation (left pair in each row) and CM excitation (right pair in each row) at $z =$ 13–18 mm and $z = 35$ mm (100 × visualization scaling).

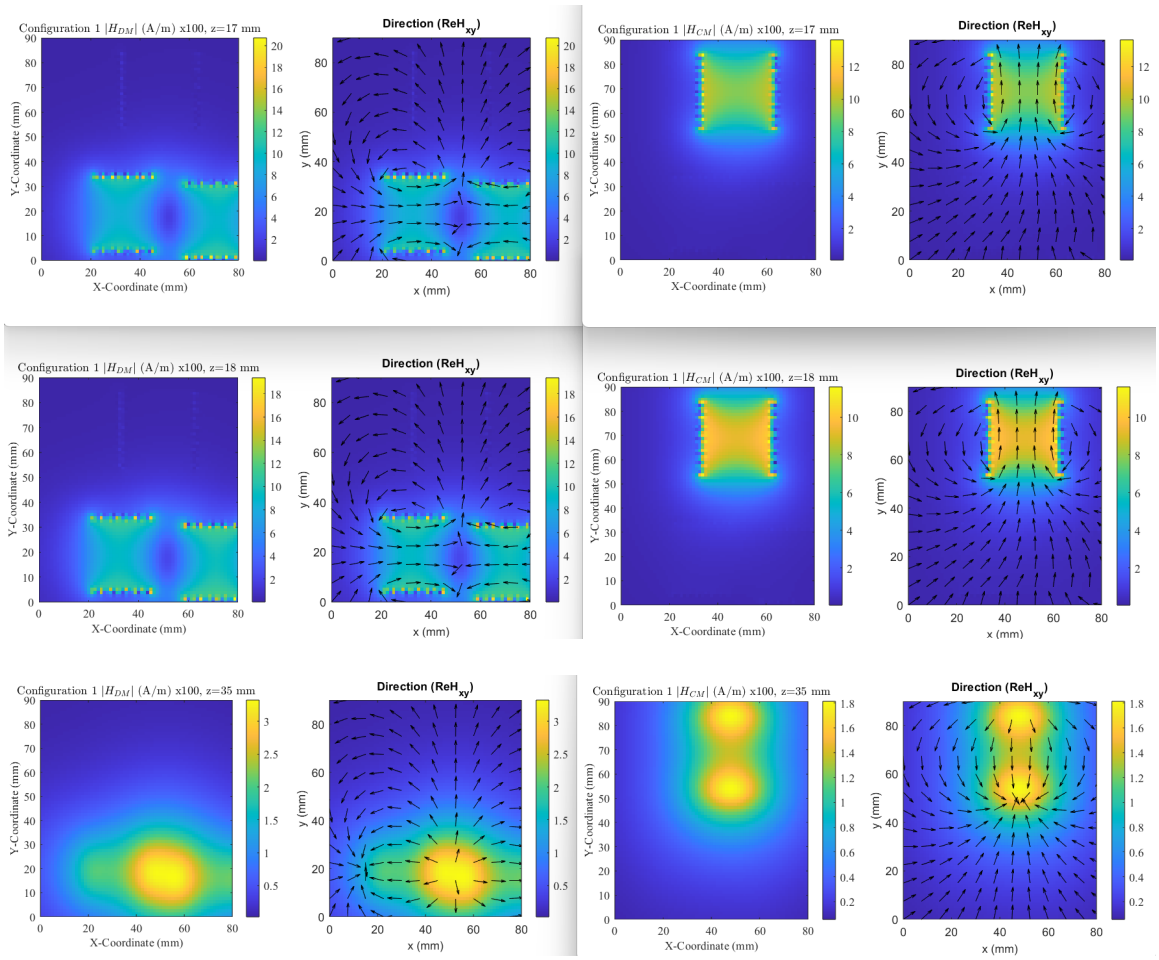


Figure 4.5. Configuration 1 simulated | $H$ | magnitude and in-plane direction maps for DM excitation (left pair in each row) and CM excitation (right pair in each row) at $z =$ 13–18 mm and $z = 35$ mm (100 × visualization scaling).

Qualitative agreement is assessed by comparing *(i)* the spatial locations of field peaks, *(ii)* the symmetry of the field distribution with respect to the PCB centerline, and *(iii)* the dominant in-plane direction of the field around each choke. For the configurations studied, the model captures the expected separation between DM-driven lobes near $L_2/L_3$ and the concentrated CM-driven field near $L_1$. Differences in absolute magnitude are expected because of probe transfer-function uncertainty and the simplified representation

of core dispersion and conductor return paths. Similar limitations, and the importance of imbalance-driven mode conversion, are emphasized in prior analyses of non-ideal EMI filters [4], [12].

## 4.4 Quantitative Measurement-to-Model Comparison

### 4.4.1 Validation Metrics

While Section 4.3 demonstrated qualitative agreement between simulated and measured near-field maps, quantitative validation is necessary to assess model accuracy across operating modes and probe heights objectively. For a given configuration and measurement plane, the measured and simulated field magnitudes, $|H_{\mathrm{meas}}(x,y)|$ and $|H_{\mathrm{sim}}(x,y)|$, are compared over a common spatial grid. Three complementary metrics are used in this work [2], [6], [7].

Peak-magnitude error is defined as the relative difference between the maximum modeled and maximum measured field magnitudes:

$$\varepsilon_{\mathrm{peak}}(\%) = 100\,\frac{\max(|H_{\mathrm{sim}}|) - \max(|H_{\mathrm{meas}}|)}{\max(|H_{\mathrm{meas}}|)} \qquad (4.2)$$

The normalized root-mean-square error (NRMSE) over all sampled grid points is computed as

$$\mathrm{NRMSE} = \frac{\sqrt{\frac{1}{N}\sum_{n=1}^{N}\left(|H_{\mathrm{sim},n}| - |H_{\mathrm{meas},n}|\right)^2}}{\max(|H_{\mathrm{meas}}|) - \min(|H_{\mathrm{meas}}|)} \qquad (4.3)$$

where $N$is the number of sampled spatial points.

In addition to magnitude-based errors, the Pearson correlation coefficient is used to quantify similarity in the spatial field pattern:

$$\rho = \frac{\sum_{n=1}^{N}\left(\mid H_{\mathrm{sim},n} \mid - \mid \bar{H}_{\mathrm{sim}} \mid\right)\left(\mid H_{\mathrm{meas},n} \mid - \mid \bar{H}_{\mathrm{meas}} \mid\right)}{\sqrt{\sum_{n=1}^{N}\left(\mid H_{\mathrm{sim},n} \mid - \mid \bar{H}_{\mathrm{sim}} \mid\right)^{2}}\sqrt{\sum_{n=1}^{N}\left(\mid H_{\mathrm{meas},n} \mid - \mid \bar{H}_{\mathrm{meas}} \mid\right)^{2}}} \tag{4.4}$$

Together, these metrics separate peak prediction accuracy, overall magnitude agreement, and similarity in the spatial distribution of the predicted and measured field maps.

Figure 4.6 consolidates a direct comparison of the measured near-field $\mid H \mid$distributions (top row) and the corresponding modeled distributions (bottom row) for each filter configuration under both DM and CM excitation [10]. After correcting the CM excitation/termination polarity to match the physical current direction, the CM field patterns show strong qualitative agreement in both hotspot location and symmetry. Residual discrepancies are most apparent in the DM cases near the choke footprints, where differences in scan height, core geometry, and as-built placement can significantly perturb the reactive near field.

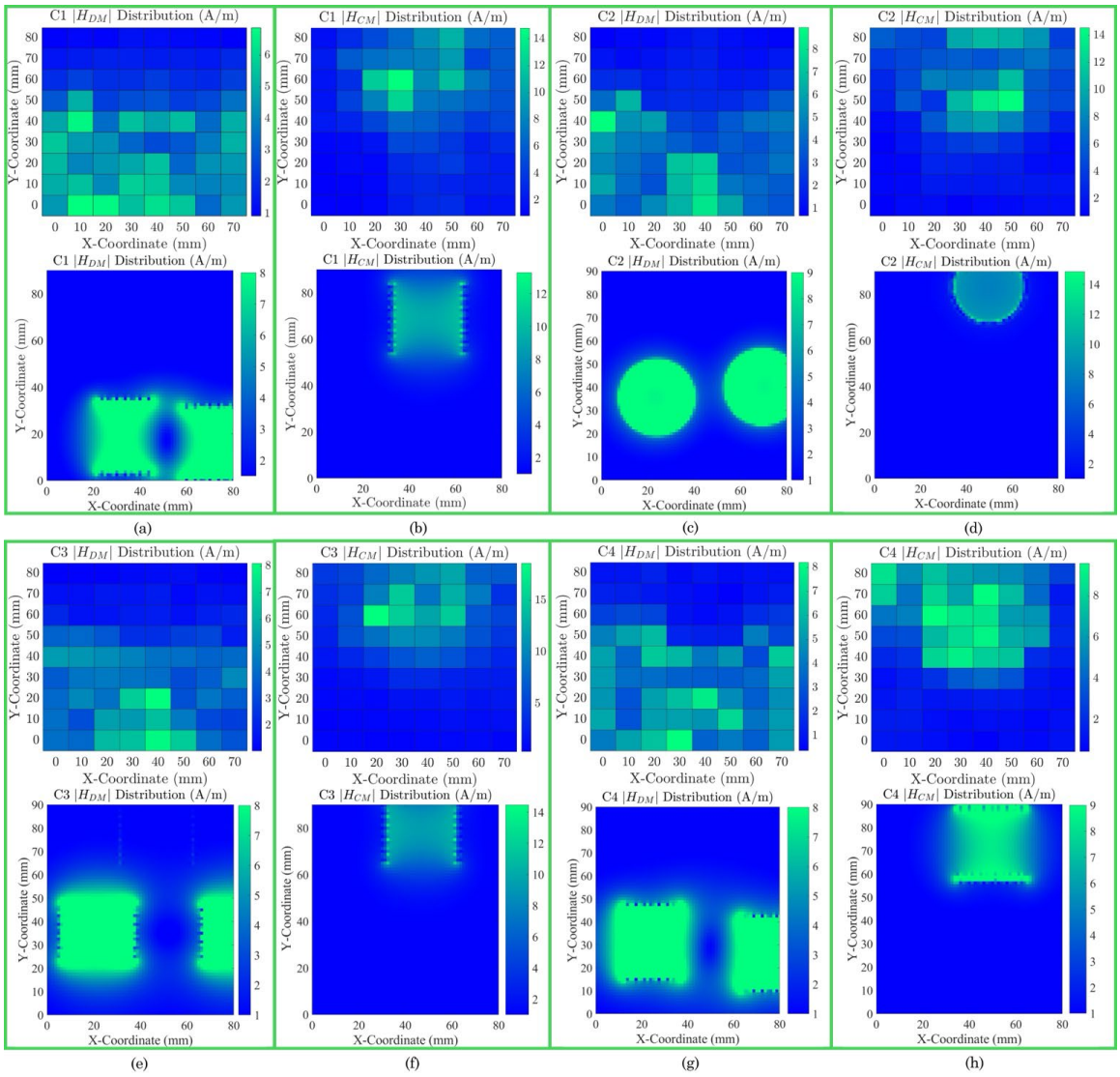


Figure 4.6. Measured (top) and modeled (bottom) | $H$ |magnitude distributions for Configurations 1–4 under DM and CM excitation. Columns correspond to (a, b) Configuration 1, (c, d) Configuration 2, (e, f) Configuration 3, and (g, h) Configuration 4; within each configuration pair, the left image shows DM excitation, and the right image shows CM excitation. Experimental scans follow the probe-clearance surface over components, whereas the model is evaluated on a constant-$z$ slice.

### 4.4.2 Interpretation and Dominant Error Sources

When interpreting measurement-to-model agreement in Fig. 4.6, several factors can drive discrepancies between the reduced-order model and measurements [4], [6], [7], [9], [10]. Segment discretization length $\Delta\ell$trades runtime for accuracy; overly coarse segmentation can under-resolve local coupling and near-field peaks. In addition, DM/CM port convention and polarity must be handled consistently. A swapped CM port polarity can invert the modeled current direction and mirror the predicted H-field distribution. After correcting the CM excitation/termination orientation, the CM maps in Fig. 4.6 match the measured symmetry and hotspot location much more closely [4], [10].

A second major source of disagreement is scan-surface mismatch. The PEEC/MoM field evaluation samples a single constant-$z$ plane, whereas the probe-to-board distance in the hardware scan varies locally because of component height. Around the DM chokes, the scan height is constrained by the $C_{DM2}$ package, while over the CMC region (except in Configuration 2) the scan height follows the common-mode choke core height [10]. As a result, the measured maps are effectively assembled from multiple local standoff distances, while the simulated maps are computed on a single observation plane. This difference can change both the apparent choke footprint and the local peak magnitude.

A related artifact occurs when the selected simulation plane intersects the ferrite volume. In that case, the modeled $|H|$ map can inherit the core cross-section, whereas the probe cannot sample inside the ferrite and instead records the external fringing field averaged over a finite aperture. Consequently, the measured contours appear smoother than the modeled contours near the core edges. Additional discrepancies also arise from effective-

permeability calibration at a single frequency, finite probe aperture and calibration uncertainty, simplified filament geometry, and millimeter-scale as-built placement tolerances.

These considerations explain why the CM agreement improved markedly after correcting the CM excitation/termination convention: once the drive condition matched the hardware, the dominant remaining differences became geometric and measurement-related rather than polarity-related. The most impactful refinements for future work are therefore improved as-built coordinate extraction, more detailed ferrite/winding geometry, and multi-height or stitched-plane field evaluation.

When interpreting measurement-to-model agreement in Fig. 4.6, several factors can drive discrepancies between the reduced-order model and measurements [6], [7], [4], [9], [10].

• Segment discretization length $\Delta\ell$ trades runtime for accuracy; overly coarse segmentation can under-resolve local coupling and near-field peaks.

• DM/CM port convention and polarity: Mode decomposition requires consistent reference directions for the CM excitation and termination currents. A swapped CM port polarity can invert the modeled current direction and mirror the predicted *H*-field distribution. After correcting the CM excitation/termination orientation, the CM maps in Fig. 4.6 match the measured symmetry and hotspot location much more closely [4], [10].

• Non-planar scan height and core slicing: The PEEC-style field evaluation samples a single constant-*z* plane, which may intersect the ferrite core volume [9]. In the hardware scan, the probe-to-board distance is constrained by local component height—around the DM chokes the scan height is set by the CDM2 package, while over the CMC region

(except Configuration 2) the scan height follows the CMC core height [10]. This effective mixing of $z$-slices can change both the apparent choke "footprint" and the local peak magnitude near the cores.

• The effective-permeability calibration ($\mu_{eff}$) is performed at 1 MHz and may not perfectly represent frequency-dependent core behavior outside the calibration point.

• Geometric simplifications and as-built tolerances: The filament representation neglects finite conductor width/thickness, via barrels, solder/lead dress, and return-path spreading. In addition, millimeter-scale placement differences between the nominal CAD geometry and the assembled hardware can shift reactive near-field hotspots, especially near the chokes.

• Finite probe aperture and calibration factors can smooth or bias the measured spatial gradients compared with point-sample simulation.

• Probe positioning and height uncertainty (±1–2 mm) can noticeably change measured magnitude in the reactive near field.

Height-dependent differences are particularly important for magnetic near-field scans because $|H|$ decays rapidly with distance from the source. The PEEC post-processing used in this work evaluates the field on a single observation plane, $z = z_{slice}$. In contrast, the experimental scan must clear components of different heights; therefore, the "constant-height" scan is effectively piecewise and can combine multiple probe standoff distances within the same map.

In the measurements used to generate Fig. 4.6, regions around the DM chokes were scanned near the height of CDM2 (set by probe clearance), while points taken directly

over the common-mode choke were acquired near the height of the CMC core surface (Configurations 1, 3, and 4). Configuration 2 is the exception because the CM region height constraint differs, so the scan height over that region does not match the other cases. This mismatch means the measured maps are not strictly taken on a single plane, while the simulated maps are, which can change the apparent footprint of each core and shift peak locations.

A second related artifact is that the chosen simulation plane can intersect the ferrite volume. When this occurs, the modeled $|H|$ map may "inherit" the core cross-section (high field inside the high-$\mu$ region), whereas the probe cannot sample inside the ferrite; the measurement therefore reflects the external fringing field and the finite probe aperture, yielding smoother contours. Future work to tighten measurement-to-model agreement should *(i)* evaluate the modeled field on multiple $z$-slices matching the experimental probe heights and stitch them using the same height mask as the scan, and *(ii)* apply a spatial averaging kernel that approximates the probe loop area and grid spacing.

These points also explain why the CM agreement improved markedly after correcting the CM excitation/termination convention: once the drive condition matched the hardware, the dominant remaining differences were geometric (scan-height topography, component placement tolerance, and simplified core/winding representation) rather than circuit polarity. If additional tuning is desired, the most impactful knobs are refining the as-built component coordinates/rotations and improving the ferrite-and-winding geometry used by the PEEC model.

## 4.5 Discussion and Model Limitations

The modeling framework intentionally simplifies several aspects of the physical system to enable rapid configuration sweeps. The most important limitations are the use of a single fitted $\mu_{\text{eff}}$ per choke at 1 MHz rather than a frequency-dispersive core model, the omission of detailed PCB trace and lead geometry, and the use of segment-level approximations for mutual inductance. Despite these simplifications, the approach provides useful engineering insight: it links observable near-field patterns to identifiable current loops and coupling paths, and it produces coupling matrices that capture the influence of compact filter-layout topology. Simplified choke models and effective-parameter approaches are widely used when balancing fidelity and computational cost in EMI-filter analysis [2], [5].

Future improvements include refining the mutual-inductance evaluation toward full Neumann-integral PEEC accuracy, incorporating additional capacitive coupling paths such as trace-to-trace and trace-to-chassis capacitances, and extending validation to additional frequencies at which magnetoquasistatic assumptions become less accurate. For PCB structures with characteristic dimensions on the order of a few centimeters to a few tens of centimeters, the MQS approximation remains well justified at low MHz frequencies, where the wavelength is still much larger than the structure. As frequency increases, however, distributed capacitance, propagation effects, and higher-order field behavior become more important, and full-wave modeling becomes increasingly necessary. These extensions are particularly relevant for capturing DM-CM

transformation and parasitic coupling effects reported in non-ideal EMI-filter studies [1], [4], [8].

A final practical limitation is scan-surface mismatch: the present validation compares simulated maps evaluated on a single constant-$z$ plane to experimental scans acquired at probe heights that vary across the board because of component-clearance constraints. Aligning the simulated evaluation surface with the local probe height, or measuring multiple constant-$z$ planes experimentally, is expected to reduce the remaining discrepancies near the choke footprints [10].

## 4.6 Circuit-Level Validation: Insertion Loss and Output Impedance

The near-field validation presented in Sections 4.2–4.5 confirms that the reduced-order MoM extraction captures the dominant spatial trends across the four hardware configurations. A complementary validation channel is agreement in frequency-domain circuit metrics that are routinely used to qualify EMI filters: insertion loss and output impedance, as described in Section 2.10. This section summarizes the coupling-driven effects observed in those metrics and relates them to the extracted loop-inductance matrices.

### 4.6.1 Expected Impact of Coupling on Insertion Loss

When mutual coupling is neglected, a parasitic EMI-filter model often predicts resonant peaks at incorrect frequencies and can underestimate the severity of anti-resonances created by interactions between inductors and capacitor ESL loops. Including the extracted mutual-inductance terms modifies the effective inductances in the DM and CM

paths, which shifts the locations of resonances and can change their damping. In compact layouts, particularly Configurations 3 and 4, stronger coupling between the DM chokes and nearby capacitor loops is expected to produce larger deviations in the DM insertion-loss curve relative to a simplified uncoupled representation. Similarly, coupling within the common-mode choke windings and between the CM choke and Y-capacitor loops can alter the CM insertion-loss response.

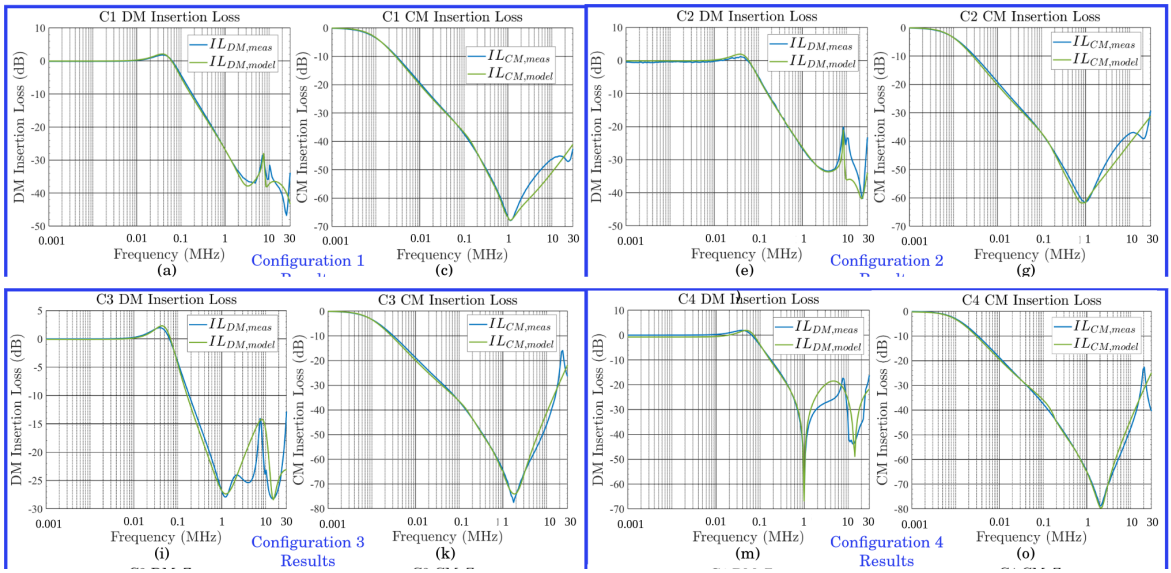


Figure 4.7. Measured versus simulated insertion loss for Configurations 1–4 in both DM and CM.

### 4.6.2 Output Impedance and Potential Filter-Converter Interaction

Output impedance provides complementary insight because it highlights resonant peaks that may interact with the converter input impedance and influence stability or emitted noise. Mutual coupling can either increase or decrease these peaks depending on the relative phase relationships among the coupled loop currents. The conference study used a $\mathbf{50\ \Omega}$ source/termination VNA setup to measure both $\boldsymbol{Z_{out,DM}}$ and $\boldsymbol{Z_{out,CM}}$, and including the extracted coupling terms improved alignment of the dominant resonances relative to a simplified uncoupled parasitic model. In the context of this thesis, these measurements provide a circuit-domain corroboration of the coupling trends inferred from the near-field maps.

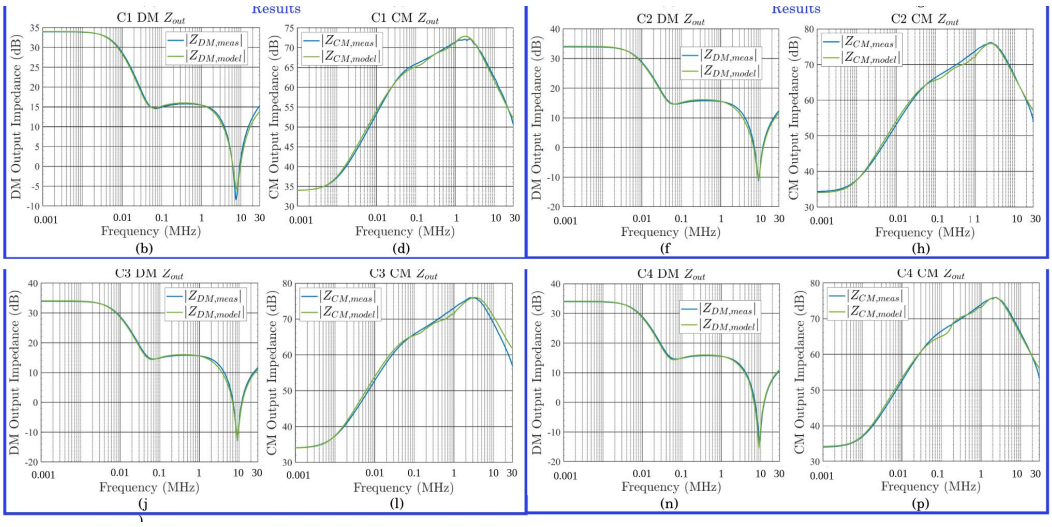


Figure 4.8. Measured versus simulated output-impedance magnitude $|\ Z_{\mathrm{out}}\ |$ for Configurations 1–4 in both DM and CM.

To quantify model accuracy across configurations, Table 4.6 reports the RMSE between measured and modeled insertion loss and output impedance in both DM and CM. Table 4.7 summarizes the dominant insertion-loss attenuation peaks and output-impedance resonance magnitudes extracted from the measurement/model comparison dataset.

Table 4.6. RMSE between measured and modeled insertion loss and output impedance for Configurations 1–4.

| EMI Filter | $IL_{DM}$ RMSE | $IL_{CM}$ RMSE | $Z_{DM}$ RMSE | $Z_{CM}$ RMSE |
|---|---|---|---|---|
| C1 | 1.348 dB | 2.102 dB | 0.555 dB | 0.509 dB |
| C2 | 2.373 dB | 1.730 dB | 0.521 dB | 0.739 dB |
| C3 | 2.280 dB | 1.951 dB | 0.501 dB | 1.149 dB |
| C4 | 2.692 dB | 2.288 dB | 0.549 dB | 0.637 dB |

Table 4.7: Dominant insertion-loss attenuation peaks and output-impedance resonance magnitudes extracted from

the Configurations 1–4 measurement/model comparison dataset.

| EMI Filter | ILDM,peak1 (dB) | ILDM,peak2 (dB) | ILDM,peak3 (dB) |
|---|---|---|---|
| C1 | -36.87 dB | -28.56 dB | -46.76 dB |
| C2 | -33.47 dB | -20.13 dB | -41.75 dB |
| C3 | -27.36 dB | -14.20 dB | -28.22 dB |
| C4 | -66.64 dB | -17.41 dB | -43.07 dB |

Table 4.7: Dominant insertion-loss attenuation peaks and output-impedance resonance magnitudes extracted from the Configurations 1–4 measurement/model comparison dataset.

| EMI Filter | ILCM,peak1 (dB) | ILCM,peak2 (dB) |
|---|---|---|
| C1 | -67.92 dB | -45.13 dB |
| C2 | -61.49 dB | -36.90 dB |
| C3 | -74.08 dB | -15.92 dB |
| C4 | -79.78 dB | -22.63 dB |

| EMI Filter | ZDM,peak (dB) | ZCM,peak (dB) |
|---|---|---|
| C1 | -8.37 dB | 72.13 dB |
| C2 | -11.21 dB | 75.91 dB |
| C3 | -12.75 dB | 76.02 dB |
| C4 | -12.92 dB | 75.91 dB |

Across configurations, including coupling terms consistently reduces mismatch to the measured responses and more accurately captures shifts in resonance locations and peak attenuation levels [10]. Because insertion loss, output impedance, and near-field magnetic radiation are all driven by the same underlying DM/CM current distributions, validating the coupling matrix against multiple metrics strengthens confidence in the model's predictive value. This multi-metric perspective is consistent with modal decomposition and coupled-circuit approaches reported in the EMI literature [3], [4], [7], [10].

# CHAPTER 5

# CONCLUSION AND FUTURE WORK

This thesis presented a magnetoquasistatic, Method-of-Moments-inspired modeling workflow for extracting magnetic coupling and predicting near-field magnetic-field distributions in EMI filter hardware. By representing the dominant current paths as segmented filamentary conductors, calibrating an effective core permeability at 1 MHz, and explicitly modeling the two windings of the common-mode choke, the method enables rapid comparison of multiple PCB layouts while retaining physically interpretable self- and mutual-inductance terms. The resulting loop-inductance matrices, coupling coefficients, near-field $H$-field maps, insertion-loss predictions, and output-impedance comparisons demonstrate that layout-dependent magnetic coupling can materially alter both circuit-level filter behavior and spatial field distributions. In this sense, the proposed approach serves as a practical intermediate layer between lumped circuit design and full three-dimensional electromagnetic analysis [8]– [10].

Future work should extend the present framework in three directions. First, a more complete capacitive extension should be incorporated so that trace-to-trace, trace-to-chassis, and lead-to-chassis electric-field couplings can be included explicitly, particularly for configurations in which imbalance-driven DM-CM transformation becomes important [1], [3], [4]. Second, ferrite modeling should be refined beyond a single fitted effective permeability at 1 MHz to include frequency dispersion and, if needed, nonlinear core behavior [5]. Third, the inductive extraction itself can be

improved by moving toward a fuller PEEC-grade evaluation of self and mutual terms while preserving the reduced-order structure needed for rapid layout sweeps [8], [9]. Additional validation at higher frequencies and with height-matched or stitched measurement planes would further clarify the range over which the present magnetoquasistatic approximation remains reliable for compact EMI-filter hardware [10]– [12].

REFERENCES


1. Y. Murata, K. Takahashi, T. Kanamoto, and M. Kubota, "Analysis of Parasitic Couplings in EMI Filters and Coupling Reduction Methods," *IEEE Transactions on Electromagnetic Compatibility*, vol. 59, no. 6, pp. 1880–1886, Dec. 2017. doi: 10.1109/TEMC.2017.2690457.
2. S. Wang, F. C. Lee, D. Y. Chen, and W. G. Odendaal, "Effects of parasitic parameters on EMI filter performance," *IEEE Transactions on Power Electronics*, vol. 19, no. 3, pp. 869–877, May 2004. doi: 10.1109/TPEL.2004.826527.
3. S. Wang and F. C. Lee, "Investigation of the Transformation Between Differential-Mode and Common-Mode Noises in an EMI Filter Due to Unbalance," *IEEE Transactions on Electromagnetic Compatibility*, vol. 52, no. 3, pp. 578–587, Aug. 2010. doi: 10.1109/TEMC.2009.2038899.
4. A. J. Roudposht, L. Illiano, X. Wu, F. Grassi, and S. A. Pignari, "Analysis and Circuit Modeling of Mode Conversion in Non-Ideal EMI Filters," *2025 International Symposium on Electromagnetic Compatibility – EMC Europe*, Paris, France, 2025, pp. 1321–1326. doi: 10.1109/EMCEurope61644.2025.11176270.
5. H. Jie, Z. Zhao, H. Li, C. Wang, Y. Chang, and K. Y. See, "Characterization and Circuit Modeling of Electromagnetic Interference Filtering Chokes in Power Electronics: A Review," *IEEE Transactions on Power Electronics*, vol. 40, no. 1, pp. 920–943, Jan. 2025. doi: 10.1109/TPEL.2024.3454152.
6. Y. Wu, K. Choksi, S. Defaz, A. B. Mirza, and F. Luo, "Modeling and Optimization of Near-Field Coupling Between Power Loop and Gate Drive in

High-Density Bidirectional Converters," *IEEE Transactions on Electromagnetic Compatibility*, vol. 67, no. 4, pp. 1334–1351, Aug. 2025. doi: 10.1109/TEMC.2025.3571381.

7. T. McGrew and Q. Li, "Effect of Magnetic Couplings on Conducted EMI of GaN-Based PFC Converter," *2025 IEEE Applied Power Electronics Conference and Exposition (APEC)*, Atlanta, GA, USA, 2025, pp. 1557–1563. doi: 10.1109/APEC48143.2025.10977111.
8. A. E. Ruehli, "Inductance calculations in a complex integrated circuit environment," *IBM Journal of Research and Development*, vol. 16, no. 5, pp. 470–481, Sept. 1972.
9. R. F. Harrington, *Field Computation by Moment Methods*. New York, NY, USA: Macmillan, 1968.
10. C. Reece, J. Sherrill, and A. Mallik, "Near-Field Magnetic Mutual Coupling Extraction and Analysis on DM/CM Conducted Emission EMI Noise Attenuation Performance in EMI Filter," submitted to the *IEEE Energy Conversion Congress and Exposition (ECCE)*, 2026.
11. H. Zhang and S. Wang, "Near Magnetic Field Assessment and Reduction for Magnetic Inductors With Magnetic Moment Analysis," *IEEE Transactions on Power Electronics*, vol. 37, no. 2, pp. 1641–1652, Feb. 2022. doi: 10.1109/TPEL.2021.3105643.

12. B. Zhang and S. Wang, "Analysis and Reduction of the Near Magnetic Field Emission From Toroidal Inductors," *IEEE Transactions on Power Electronics*, vol. 35, no. 6, pp. 6251–6268, June 2020. doi: 10.1109/TPEL.2019.2953748.
13. D. Xie and X. Zhou, "Mutual Inductance Extraction-Based Radiated EMI Modeling for Integrated Power Converter and Passive Component Under Different Relative Positions and Orientations," in *Proc. 8th IEEE Int. Autom. Electr. and Auto. Control Conf. (IAEAC)*, May 2025, pp. 864–869. doi: 10.1109/IAEAC61931.2025.10903589.
14. Ansys, Inc., *Q3D Getting Started LE05: Inductance Matrix Reduction*, Release 2020 R1, 2020. [Online]. Available: Ansys Innovation Space, "Q3D_GS_2020R1_EN_LE05_Ind_Matrix.pdf."
15. D. Romano, G. Pettanice, M. Stumpf, I. E. Lager, *et al.*, "Partial element equivalent circuit modeling of distributed and lumped time-varying dielectric phenomena," *Scientific Reports*, vol. 15, 2025, Fig. 1. doi: 10.1038/s41598-025-27863-4.
16. E. Sicard and A. Boyer, *IC-EMC User's Manual*, Version 2.5. Toulouse, France: INSA Toulouse, 2011, Fig. 18-1.
17. D. M. Gamage, M. Ranasinghe, and V. Dinavahi, "Applications of the partial element equivalent circuit method in computational electromagnetics simulation: An overview," *Electric Power Systems Research*, vol. 243, Art. no. 111487, 2025, doi: 10.1016/j.epsr.2025.111487.

18. COMSOL AB, “Introductory Guide to Field Electromagnetics and Theory,” *COMSOL Multiphysics Cyclopedia*. [Online]. Available: https://www.comsol.com/multiphysics/electromagnetics. Accessed: April 4, 2026.

# APPENDIX A

## SUPPLEMENTARY GOVERNING RELATIONS FROM PEEC/MOM LITERATURE

This appendix collects supplementary relations from the PEEC, Method-of-Moments (MoM), mixed-mode network, and magnetoquasistatic (MQS) literature that provide theoretical context for the reduced-order model developed in Chapter 2. These relations are included for completeness and to indicate possible directions for future extensions, particularly capacitive extraction and retarded-kernel formulations. They are not all used directly in the implemented reduced-order workflow [5], [8], [9].

## A.1 Magnetoquasistatic Background

In phasor form, Maxwell's equations may be written as

$$\nabla \times \mathrm{E} = -j\omega \mathrm{B}, \nabla \times \mathrm{H} = \mathrm{J} + j\omega \mathrm{D}, \nabla \cdot \mathrm{D} = \rho_v, \nabla \cdot \mathrm{B} = 0 \qquad \text{(A.1)}$$

with the constitutive relations

$$\mathrm{B} = \mu \mathrm{H}, \mathrm{D} = \epsilon \mathrm{E}, \mathrm{J} = \sigma \mathrm{E} \qquad \text{(A.2)}$$

Under MQS conditions, displacement-current and retardation effects are negligible when the electrical dimensions are sufficiently small, which is commonly expressed by

$$k_0 L_{\max} \ll 1, k_0 R \ll 1, k_0 = \frac{\omega}{c} = \frac{2\pi}{\lambda} \qquad \text{(A.3)}$$

In the present thesis, these conditions justify the use of static inductive kernels for the low-MHz EMI-filter structures of interest [8], [9].

## A.2 Charge-Based PEEC Background

Classical PEEC formulations may include not only partial inductances but also charge-based electric-field coupling through a coefficient-of-potential matrix. In a simplified panel-based formulation, the nodal potential vector vand charge vector qare related by

$$\mathrm{v} = \mathrm{P}\mathrm{q}, \qquad \text{(A.4)}$$

so that

$$\mathrm{q} = \mathrm{C}\mathrm{v}, \mathrm{C} = \mathrm{P}^{-1} \qquad \text{(A.5)}$$

These relations are included here to clarify what is omitted in the present thesis: the implemented model focuses on inductive coupling and does not perform a full coefficient-of-potential or capacitive PEEC extraction [5], [8].

## A.3 Reduction and Numerical Properties of the Coupled System

When a coupled impedance system is partitioned into retained and eliminated variables, the reduced impedance seen by the retained variables is obtained through a Schur complement (Kron reduction). For the partition

$$\begin{bmatrix} \mathrm{v}_1 \\ \mathrm{v}_2 \end{bmatrix} = \begin{bmatrix} \mathrm{Z}_{11} & \mathrm{Z}_{12} \\ \mathrm{Z}_{21} & \mathrm{Z}_{22} \end{bmatrix} \begin{bmatrix} \mathrm{i}_1 \\ \mathrm{i}_2 \end{bmatrix},$$

the reduced impedance is

$$\mathrm{Z_{red}} = \mathrm{Z_{11}} - \mathrm{Z_{12}}\mathrm{Z_{22}^{-1}}\mathrm{Z_{21}} \qquad \text{(A.6)}$$

If $\mathrm{v_2} = 0$, then $i_2 = -Z_{22}^{-1}Z_{21}i_1$, and the remaining variables satisfy $\mathrm{v_1} = Z_{red}i_1$ [3], [7]. Because the underlying magnetostatic kernels are reciprocal, assembled inductance and impedance matrices should be symmetric up to numerical error. A common stabilization is therefore to enforce symmetry explicitly:

$$\mathrm{Z_{sym}} = \frac{1}{2}(\mathrm{Z}+\mathrm{Z}^T) \qquad \text{(A.7)}$$

At MHz frequencies, conductor loss is often approximated using the skin-depth relation

$$\delta = \sqrt{\frac{2\rho}{\omega\mu}} = \sqrt{\frac{\rho}{\pi f\mu}}, \qquad \text{(A.8)}$$

where $\rho$ is the conductor resistivity and $\mu$is the magnetic permeability [8].

For a long straight round conductor of length $\ell$and radius $a$, with $\ell \gg a$, one commonly used self-inductance approximation is

$$L_{\mathrm{self}} \approx \frac{\mu_0\ell}{2\pi}\left[\ln\left(\frac{2\ell}{a}\right) - \frac{3}{4}\right] \qquad \text{(A.9)}$$

This type of expression motivates the use of closed-form self-term approximations in filament and partial-inductance methods [5], [8].

## A.4 Mixed-Mode Quantities and Mode Conversion

For conducted-EMI interpretation, terminal quantities may be transformed into differential-mode (DM) and common-mode (CM) wave variables. Using single-ended incident and reflected waves $(a_1, a_2)$ and $(b_1, b_2)$, the mixed-mode wave definitions are

$$a_d = \frac{a_1 - a_2}{\sqrt{2}}, a_c = \frac{a_1 + a_2}{\sqrt{2}}, b_d = \frac{b_1 - b_2}{\sqrt{2}}, b_c = \frac{b_1 + b_2}{\sqrt{2}} \qquad \text{(A.10)}$$

The corresponding mixed-mode S-parameter relation is

$$\begin{bmatrix} b_d \\ b_c \end{bmatrix} = \begin{bmatrix} S_{dd} & S_{dc} \\ S_{cd} & S_{cc} \end{bmatrix} \begin{bmatrix} a_d \\ a_c \end{bmatrix} \qquad \text{(A.11)}$$

In this representation, $S_{cd}$ quantifies differential-to-common conversion and $S_{dc}$ quantifies common-to-differential conversion. These quantities are useful when assessing imbalance-driven mode conversion in practical EMI filters [3], [4].

## A.5 Magnetic Moment, Energy, and Retarded Kernels

Magnetic-moment analysis provides a reduced interpretation of near-field radiation from current loops and toroidal structures. For $N$ turns carrying current $I$, enclosing area $A$, with unit normal $\hat{\mathrm{n}}$, the equivalent magnetic dipole moment is

$$m = NIA\,\hat{\mathrm{n}} \qquad \text{(A.12)}$$

In the dipole approximation, the magnetic-field intensity is

$$\mathrm{H(r)} = \frac{1}{4\pi r^3}[3(\mathrm{m}\cdot\hat{\mathrm{r}})\hat{\mathrm{r}} - \mathrm{m}] \qquad \text{(A.13)}$$

This viewpoint is useful for interpreting how winding orientation affects the observed near-field pattern [11], [12].

For inductive extraction methods such as PEEC and MoM, the loop flux-linkage vector and stored magnetic energy provide useful physical checks on matrix symmetry and passivity:

$$\lambda = Li, \qquad \textit{(A.14)}$$

$$W_m = \frac{1}{2} i^T L i \qquad \textit{(A.15)}$$

Under full-wave PEEC formulations, retardation may be incorporated by replacing the static $1/R$kernel with the frequency-dependent kernel $e^{-jk_0R}/R$. For a filament pair, the retarded magnetic vector potential contribution may be written as

$$\mathrm{A}_n(\mathrm{r}_m) = \frac{\mu_0}{4\pi}\int_{\ell_n} \frac{I_n e^{-jk_0R_{mn}}}{R_{mn}}\, d\ell_n \qquad \text{(A.16)}$$

Under MQS conditions, $k_0R_{mn} \ll 1$, so $e^{-jk_0R_{mn}} \approx 1$, and Eq. (A.16) reduces to the static Neumann-kernel form used in Chapter 2 [8], [9].

Taken together, Eqs. (A.4) – (A.5) highlight the capacitive extraction omitted in the present thesis, Eqs. (A.10) – (A.11) summarize the mixed-mode framework relevant to

DM↔CM conversion, and Eqs. (A.14) – (A.16) provide complementary energy and full-wave background relations that motivate inductance-matrix symmetry, passivity, and the MQS static-kernel approximation.

# APPENDIX B:

# REDUCED-ORDER MOM MATLAB IMPLEMENTATION, MODEL PROPERTIES, AND GOVERNING EQUATIONS

## B.1 Purpose and Novelty of the MATLAB Implementation

The in-house written MATLAB script implements the reduced-order electromagnetic modeling framework developed in this thesis. The purpose of the code is not simply to calculate inductance values or generate magnetic field plots. Its main contribution is that it provides a layout-aware reduced-order modeling approach that bridges the gap between conventional lumped-element EMI filter analysis and computationally expensive full-wave electromagnetic simulation.

Traditional EMI filter analysis often treats the common-mode choke, differential-mode chokes, and capacitors as idealized lumped elements connected by an abstract schematic. While this is useful for circuit-level analysis, it does not directly capture the physical placement, orientation, current-loop geometry, and parasitic magnetic coupling paths that arise in a compact EMI filter layout. Prior EMI-filter studies have shown that these non-idealities can shift resonance frequencies, reduce insertion loss, and promote differential-mode/common-mode mode conversion [1]– [5].

The novelty of this MATLAB implementation is that it preserves the most important physical electromagnetic features of the filter layout while reducing the problem to a compact circuit-domain representation. The physical EMI filter geometry is discretized into current-carrying filament segments. A Method-of-Moments-style magnetoquasistatic coupling kernel is then used to evaluate segment-to-segment inductive interactions. These segment-level interactions are aggregated into a reduced loop-level inductance matrix

that can be solved efficiently in the circuit domain and then reused to reconstruct magnetic near-field behavior.

Therefore, the proposed model provides a reduced-order, layout-aware alternative to both simplified lumped circuit models and full-wave electromagnetic solvers. It is computationally lightweight enough for configuration sweeps and design comparison but physically detailed enough to capture the dominant inductive coupling and near-field behavior introduced by real component placement. This follows the same motivation stated in the thesis: the approach is meant to operate as an intermediate layer between circuit-level EMI filter synthesis and layout-resolved electromagnetic analysis, without requiring repeated full three-dimensional meshing for every layout perturbation [8], [9].

The script explicitly models the common-mode choke as two separate windings, *L1P* and *L1N*, rather than collapsing the common-mode choke into a single equivalent current loop. This allows the measured or simulated positive and negative winding currents to be applied directly in both differential-mode and common-mode excitation cases. This is important because imbalance and parasitic coupling can create cross-mode transfer paths that are not represented if the common-mode choke is treated as a single ideal element [3]– [5].

## B.2 Overview of the Modeling Pipeline

The reduced-order modeling process implemented in MATLAB follows the sequence:

The workflow can be summarized as follows:

1. Define the physical EMI filter geometry from component dimensions, PCB coordinates, and photo-calibrated placement.
2. Represent toroidal windings and capacitor current paths using straight filament segments.
3. Build a segment-level complex impedance matrix using magnetoquasistatic self- and mutual-inductance approximations.
4. Add conductor loss using a skin-depth-based AC resistance approximation.
5. Group segments into physical loop objects.
6. Aggregate segment-level inductances into a reduced loop-level inductance matrix.
7. Solve loop currents for differential-mode and common-mode excitation cases.
8. Reconstruct magnetic near fields above the PCB using a finite straight-segment Biot–Savart expression.
9. Export loop inductances, mutual inductances, coupling coefficients, and field plots.

This workflow retains the physical geometry-to-circuit connection that is usually lost in a purely lumped schematic model. It is also consistent with the PEEC/MoM viewpoint, where electromagnetic interactions are discretized into matrix form and then mapped into a circuit-compatible representation [8], [9].

## B.3 Geometry Representation

Each conductor path is represented as a set of straight filament segments. A segment ($m$) is defined by a start point, end point, length, midpoint, and unit direction vector:

$$\mathrm{r}_{m,e} = [x_{m,e} \quad y_{m,e} \quad z_{m,e}]$$

$$\ell_m = \| \mathrm{r}_{m,e} - \mathrm{r}_{m,s} \|$$

$$\hat{\mathrm{u}}_m = \frac{\mathrm{r}_{m,e} - \mathrm{r}_{m,s}}{\ell_m}$$

$$\mathrm{r}_{m,\mathrm{mid}} = \frac{\mathrm{r}_{m,s} + \mathrm{r}_{m,e}}{2}$$

The toroidal choke windings are approximated as stacked circular filament loops using the mean toroid diameter. The loop planes are rotated according to the measured or estimated physical orientation of each choke in the PCB configuration. Capacitor current paths are represented as simplified rectangular loop structures between their terminal coordinates.

The full topology contains eight loop groups:

*{L1P, L1N, L2DM, L3DM, C1_1, C4_1, C2, C3}*

where *L1P* and *L1N* are the two common-mode choke windings, and $L3_{\mathrm{DM}}$ are the differential-mode chokes, and $C1\_1$, $C4\_1$, $C2$, and $C3$ are capacitor current-loop approximations.

This geometry representation is central to the novelty of the method. Rather than volumetrically meshing the full PCB, ferrite cores, air region, and conductor cross sections, the implementation keeps only the dominant current-carrying paths that govern low-MHz magnetic near-field coupling. This is consistent with the thesis assumption that the relevant behavior is magnetoquasistatic and dominated by inductive loop-to-loop interaction [8], [9].

B.4 Segment-Level MoM Impedance Matrix

The MATLAB model constructs a complex segment-level impedance matrix:

where $R$ is the conductor resistance contribution and $L_{seg}$ is the segment-level partial inductance matrix.

The approximate self-impedance of segment $m$is modeled using a straight-wire partial inductance expression:

$$Z_{mm} = j\omega \frac{\mu_{\text{self},m}\ell_m}{2\pi}\left[\ln\left(\frac{2\ell_m}{a}\right) - 1\right]$$

where $a$ is the effective wire radius, $\ell_m$ is the segment length, and $\mu_{\text{self},m}$ is the effective permeability assigned to the segment group.

The mutual impedance between segments $m$and $n$is approximated as:

$$Z_{mn} = j\omega \frac{\mu_{\text{eff},mn}}{4\pi}\frac{\ell_m \ell_n}{R_{mn}}\cos\,\theta_{mn}$$

where

$$R_{mn} = \| \mathrm{r}_{m,\text{mid}} - \mathrm{r}_{n,\text{mid}} \|$$

and

$$\cos\,\theta_{mn} = \hat{\mathrm{u}}_m \cdot \hat{\mathrm{u}}_n$$

This expression captures the dominant magnetoquasistatic coupling between current-carrying filament segments. Parallel nearby segments have stronger positive mutual coupling, oppositely directed nearby segments can produce negative coupling, and perpendicular segments contribute weakly because the dot product term is small.

The formulation is consistent with the PEEC/MoM foundation used in prior work, where conductor geometry is discretized into basis elements and the resulting electromagnetic interactions are assembled into impedance or partial-inductance matrices [8], [9].

A minimum-distance regularization is applied to avoid singular behavior when two segment midpoints are very close:

$$R_{mn} \leftarrow \max\left(R_{mn}, R_{\min}\right)$$

After matrix construction, the code enforces symmetry to preserve reciprocal inductive coupling:

$$Z_{mn} = Z_{nm}$$

This step reduces numerical asymmetry introduced by finite precision and near-singular geometric interactions.

B.5 Effective Permeability Calibration

The model does not solve the full magnetic material boundary-value problem inside the toroidal cores. Instead, each choke group is assigned an effective relative permeability that is calibrated to match target inductance values.

First, the segment-level inductance matrix is extracted from the imaginary part of the impedance matrix:

First, the segment-level inductance matrix is extracted from the imaginary part of the impedance matrix:

$$\mathbf{L}_{\text{seg}} = \frac{\text{Im}\{\mathbf{Z}\}}{\omega}$$

For an isolated coil, the model inductance is computed by summing all segment interactions within that coil:

$$L_{\text{model}} = \sum_{m} \sum_{n} L_{\text{seg},mn}$$

The effective relative permeability is then scaled as:

$$\mu_{r,\text{eff}} = \mu_{r,\text{guess}} \frac{L_{\text{target}}}{L_{\text{model}}}$$

The script uses this calibration to force the simplified filament-based winding model to match the target common-mode and differential-mode choke inductances. This is a practical reduced-order treatment: the magnetic core is not solved with full field fidelity, but its dominant inductive effect is retained through a calibrated permeability factor. This is appropriate for the thesis objective because the model is not intended to resolve every local field variation inside the ferrite core; it is intended to capture the dominant coupling quantities that affect EMI filter behavior.

For the full-topology implementation, the target values are:

$$L_{\text{CM,target}} = 261.93\ \mu\text{H}$$

$$L_{\text{DM,target}} = 11.334\ \mu\text{H}$$

The calibrated effective permeability values are then used when constructing the full EMI filter configuration.

## B.6 AC Resistance Approximation

Conductor loss is included using a skin-depth-based AC resistance approximation. The skin depth is calculated as:

$$\delta = \sqrt{\frac{\rho_{\text{Cu}}}{\pi f \mu_0}}$$

The resistance per unit length is approximated by:

$$R_s = \frac{\rho_{\text{Cu}}}{2\pi a \delta}$$

where $\rho_{\text{Cu}}$ is the resistivity of copper and $a$is the effective wire radius.

The resistance contribution of each segment is added to the diagonal of the impedance matrix:

$$Z_{mm} \leftarrow Z_{mm} + R_s \ell_m$$

This adds conductor loss while preserving the inductive coupling structure in the off-diagonal matrix terms. Detailed proximity-effect and cross-sectional current

redistribution are not solved explicitly; instead, they are absorbed into the reduced-order resistance and effective-parameter treatment. This is consistent with the computational goal of the model: retain dominant low-MHz inductive coupling while avoiding full volumetric conductor meshing.

## B.7 Loop-Level Matrix Reduction

The central reduced-order step is the aggregation of segment-level inductances into loop-level inductances. Once the segment-level inductance matrix is obtained,

$$\mathbf{L}_{\text{seg}} = \frac{\text{Im}\{\mathbf{Z}\}}{\omega}$$

segments are grouped into physical circuit loops. If loop $a$contains segment index set $\mathcal{G}_a$, and loop $b$ contains segment index set $\mathcal{G}_b$, then the reduced loop-matrix entry is:

$$L_{\text{loop},ab} = \sum_{m\in\mathcal{G}_a} \sum_{n\in\mathcal{G}_b} L_{\text{seg},mn}$$

Equivalently, using a segment-to-loop incidence matrix **B**,

$$\text{L}_{\text{loop}} = \text{B}^T \text{L}_{\text{seg}} \text{B}$$

This produces the compact loop-level inductance matrix:

$$\mathbf{L}_{\text{loop}} = \begin{bmatrix} L_{11} & M_{12} & \cdots & M_{1N} \\ M_{21} & L_{22} & \cdots & M_{2N} \\ \vdots & \vdots & \ddots & \vdots \\ M_{N1} & M_{N2} & \cdots & L_{NN} \end{bmatrix}$$

The diagonal terms are loop self-inductances, and the off-diagonal terms are mutual inductances between loop groups.

The coupling coefficient between loops $i$and $j$is calculated as:

$$k_{ij} = \frac{M_{ij}}{\sqrt{L_{ii}L_{jj}}}$$

This reduction is one of the most important parts of the thesis model. It converts a large physical segment interaction problem into a compact matrix that can be interpreted and solved like a circuit while still retaining layout-dependent electromagnetic coupling. This is also what makes the model useful for comparing configurations: off-diagonal terms directly reveal which loop pairs are strongly coupled and how that coupling changes when component placement or orientation changes.

B.8 Circuit-Domain Solution

The reduced loop-level circuit matrix is formed as:

$$\mathrm{Z}_{\text{loop}} = \mathrm{j}\omega\mathrm{L}_{\text{loop}} + \mathrm{diag}\left(\mathrm{R}_{\text{loop}} + \mathrm{Z}_{\text{cap}}\right)$$

where $\mathrm{R}_{\text{loop}}$is the loop resistance vector and $\mathrm{Z}_{\text{cap}}$ contains the capacitor loop impedances.

Each capacitor branch is modeled as a series combination of ESR, ESL, and capacitance:

$$Z_C = R_{\mathrm{ESR}} + j\omega L_{\mathrm{ESL}} + \frac{1}{j\omega C}$$

In the present implementation, $R_{\mathrm{ESR}}$ is set to zero, while capacitor ESL and capacitance values are assigned to the capacitor loop groups.

The loop current vector is divided into known and unknown components:

$$\mathrm{I} = \begin{bmatrix} \mathrm{I}_k \\ \mathrm{I}_u \end{bmatrix}$$

where $\mathrm{I}_k$ contains imposed choke-loop currents and $\mathrm{I}_u$ contains unknown capacitor-loop currents.

With no independent voltage source applied to the unknown capacitor loops, the unknown currents are solved using the partitioned system:

$$\mathrm{I}_u = -\mathrm{Z}_{uu}^{-1}\mathrm{Z}_{uk}\mathrm{I}_k$$

This procedure is applied separately for differential-mode and common-mode excitation cases. The use of known measured or simulated phasor currents allows the reduced-order electromagnetic model to connect directly to circuit-level excitation conditions.

The imposed current magnitudes are converted from dB relative to 1 A:

$$|\ I\ | = I_{\mathrm{ref}} 10^{I_{\mathrm{dB}}/20}$$

with

$$I_{\text{ref}} = 1\ \text{A}$$

The complex current phasor is then formed as:

$$I = | I | e^{j\phi}$$

where $\phi$ is the current phase angle in radians.

B.9 Near-Field Reconstruction

After solving the loop currents, each loop current is assigned to the filament segments belonging to that loop. The magnetic near field is then evaluated above the PCB using a finite straight-segment Biot–Savart formulation.

For a segment with current $I_m$, unit direction vector $\hat{\mathrm{u}}_m$, start point $\mathrm{a}_m$, and length $\ell_m$, the vector from the segment start to the observation point $\mathrm{r}$ is:

$$\mathrm{R}_a = \mathrm{r} - \mathrm{a}_m$$

The axial projection along the segment is:

$$s_0 = \hat{\mathrm{u}}_m \cdot \mathrm{R}_a$$

The perpendicular displacement from the segment axis is:

$$\mathrm{R}_\perp = \mathrm{R}_a - s_0 \hat{\mathrm{u}}_m$$

with distance regularization:

$$R_{\perp}^{2} \leftarrow \max\left(\| \mathrm{R}_{\perp} \|^{2}, R_{\min}\right)$$

The finite-segment factor is:

$$F = \frac{s_0}{\sqrt{R_{\perp}^{2} + s_0^{2}}} - \frac{s_0 - \ell_m}{\sqrt{R_{\perp}^{2} + (s_0 - \ell_m)^{2}}}$$

The magnetic field contribution from segment $m$is then:

$$\mathrm{H}_m(\mathrm{r}) = \frac{I_m}{4\pi} \frac{\hat{\mathrm{u}}_m \times \mathrm{R}_{\perp}}{R_{\perp}^{2}} F$$

The total field is obtained by superposition:

$$\mathrm{H}(\mathrm{r}) = \sum_{m=1}^{N_{\mathrm{seg}}} \mathrm{H}_m\,(\mathrm{r})$$

The field magnitude is computed as:

$$|\, H \,| = \sqrt{|\, H_x \,|^2 + |\, H_y \,|^2 + |\, H_z \,|^2}$$

The corresponding air magnetic flux density estimate is:

$$|\, B_{air} \,| = \mu_0 \,|\, H \,|$$

The field is evaluated on a rectangular grid above the PCB at selected heights. In the script, these include:

$$z = 13\ mm, 14\text{–}18\ mm, 35\ mm$$

This field reconstruction step is important because it allows the reduced-order circuit solution to be connected back to measurable magnetic near-field behavior. Near-field scanning and magnetic-field mapping are commonly used to evaluate magnetic emission patterns around inductors, toroidal structures, and power-electronic assemblies [11], [12].

B.10 Optional Probe Conversion

The script also includes optional conversion functions between magnetic field magnitude and the voltage that would be induced in an ideal small-loop magnetic-field probe.

For a loop probe with $N$turns and area $A_{\text{loop}}$, the RMS probe voltage is approximated as:

$$V_{\text{rms}} = \omega \mu_0 N A_{\text{loop}} \mid H \mid$$

The equivalent value in dB$\mu$V is:

$$\text{dB}\mu\text{V} = 20\log_{10}\left(\frac{V_{\text{rms}}}{1\ \mu\text{V}}\right)$$

The inverse conversion is:

$$\mid H \mid = \frac{10^{\text{dB}\mu\text{V}/20} \cdot 10^{-6}}{\omega \mu_0 N A_{\text{loop}}}$$

These functions are included for comparison with magnetic probe measurements, although the default field plots are generated in A/m unless probe conversion is explicitly enabled.

## B.11 Numerical Stability Controls

The reduced-order implementation includes several numerical controls to improve reliability.

### B.11.1 Minimum-Distance Regularization

The mutual coupling expression contains a $1/R$-type dependence. To prevent singular or unrealistically large values when two segment midpoints are very close, the distance is regularized:

$$R_{mn} \leftarrow \max\left(R_{mn}, R_{\min}\right)$$

A similar regularization is used in the Biot–Savart near-field calculation for the perpendicular distance from an observation point to a segment.

### B.11.2 Symmetry Enforcement

Because magnetoquasistatic inductive coupling is reciprocal, the impedance matrix should be symmetric:

$$Z_{mn} = Z_{nm}$$

The MATLAB implementation enforces matrix symmetry after assembly to reduce numerical asymmetry caused by rounding or near-singular interactions.

Before solving a linear system, the code checks the reciprocal condition number. If the matrix is poorly conditioned, a small diagonal perturbation is added:

$$A \leftarrow A + \epsilon s I$$

where $s$ is based on the average diagonal magnitude and $\epsilon$ is a small scaling factor. This improves numerical robustness for nearly singular systems.

These numerical controls are practical implementation choices. They do not change the physical purpose of the model; rather, they prevent singular or ill-conditioned behavior in a thin-wire reduced-order representation.

## B.12 Why a Reduced-Order MoM Approach Is Preferred Over a Full-Wave Solver

A full-wave electromagnetic solver is not required for the objective of this thesis because the EMI filter layouts studied here operate in a regime where the dominant physical behavior is governed by magnetoquasistatic inductive coupling rather than wave propagation, far-field radiation, or distributed transmission-line effects. The physical dimensions of the filter are small compared with the electromagnetic wavelength over the frequency range of interest, so the most important coupling mechanisms are the self-inductance of local current paths, mutual inductance between nearby loops, and layout-dependent magnetic near-field interaction [8], [9].

A full-wave solver provides a more general electromagnetic solution, but that generality introduces significant modeling and computational overhead. Full-wave simulation typically requires detailed 3D geometry preparation, meshing, material assignment, boundary-condition setup, convergence checks, and repeated solves for each layout configuration. For this thesis, that level of complexity is not necessary because the research question is focused on how component placement, winding orientation, loop geometry, and parasitic inductive coupling affect EMI filter behavior across multiple physical configurations.

The reduced-order MoM implementation is better suited to this objective because it preserves the layout features that matter most while avoiding unnecessary full-wave complexity. The MATLAB model retains the physical locations and orientations of the common-mode choke, differential-mode chokes, and capacitor loops. These physical features are converted into filament segments, evaluated using a magnetoquasistatic coupling kernel, and then aggregated into a compact loop-level inductance matrix. This gives the model a direct physical interpretation: each matrix entry corresponds to a self- or mutual-inductance relationship between actual layout current paths.

Importantly, the reduced-order approach can provide accuracy comparable to a full-wave solver for the dominant magnetoquasistatic coupling quantities of interest when the operating regime remains electrically small and the model is calibrated to the relevant component inductances. This comparison is not intended as a universal statement that the reduced-order model can replace full-wave simulation in all cases. Rather, it applies to the specific quantities evaluated in this thesis: dominant loop self-inductances, mutual

inductances, coupling coefficients, circuit-domain current interactions, and magnetic near-field trends above the PCB.

The model achieves this practical accuracy by matching the dominant physics to the problem scale. The effective permeability calibration forces the simplified filament representation to match the target common-mode and differential-mode choke inductances. The segment-level MoM kernel then captures geometry-dependent mutual coupling between physical current paths. Finally, the finite straight-segment Biot–Savart calculation reconstructs the magnetic near-field distribution from the solved loop currents. For compact EMI filter layouts where inductive coupling dominates, this allows the reduced-order model to reproduce the same layout-dependent trends that a full-wave solver would identify, while requiring far less setup time and computational cost.

This accuracy claim is supported by the measurement-to-model comparisons presented in Chapter 4, including the measured and modeled near-field maps and the circuit-level insertion-loss/output-impedance comparisons. The Chapter 4 validation results show that the coupling-informed reduced-order model captures the dominant resonance shifts and configuration-dependent behavior more effectively than an uncoupled lumped model.

This approach is particularly useful because EMI filter layout design often requires comparison rather than a single high-fidelity simulation. A full-wave solver may be useful for final verification, but it is not ideal for rapidly evaluating many geometry changes or for identifying which physical coupling paths dominate the behavior. In contrast, the reduced-order MATLAB implementation can quickly compare configurations, extract loop-to-loop coupling coefficients, identify strong mutual

coupling paths, and generate magnetic field maps for both differential-mode and common-mode excitation cases.

The reduced-order approach is also more transparent than a full-wave black-box simulation. In a full-wave solver, the final field distribution may be accurate, but it can be difficult to directly identify which loop interaction, or component placement caused a specific coupling trend. In the proposed MATLAB model, the loop-level matrix explicitly exposes the coupling terms:

$$\mathbf{L}_{\text{loop}} = \begin{bmatrix} L_{11} & M_{12} & \cdots & M_{1N} \\ M_{21} & L_{22} & \cdots & M_{2N} \\ \vdots & \vdots & \ddots & \vdots \\ M_{N1} & M_{N2} & \cdots & L_{NN} \end{bmatrix}$$

where the diagonal terms represent self-inductances and the off-diagonal terms represent mutual inductances between physical loop groups. The coupling coefficient,

$$k_{ij} = \frac{M_{ij}}{\sqrt{L_{ii}L_{jj}}},$$

provides a compact measure of how strongly two physical loops interact. This makes the model useful not only for prediction, but also for design interpretation.

Therefore, the reduced-order MoM approach is preferred in this thesis because it provides the correct level of model fidelity for the problem being studied. It is more physically informative than a lumped-element schematic, more computationally efficient than a full-wave solver, and more directly tied to the layout-dependent coupling mechanisms that

influence EMI filter behavior. While a full-wave solver may provide greater generality, the reduced-order model provides comparable practical accuracy for the dominant inductive coupling and near-field trends that are central to this work.

A full-wave solver would only be necessary if the research objective required resolving effects outside the scope of the present model, such as radiation, retardation, detailed magnetic core field distributions, frequency-dependent material dispersion, complex conductor surface-current redistribution, or high-frequency wave effects. Since the thesis focuses on compact EMI filter layouts, magnetoquasistatic coupling, loop-level parasitic interaction, and near-field trends, the reduced-order MoM formulation is the more appropriate and efficient modeling choice.

## B.13 Model Outputs

The primary outputs of the MATLAB implementation are:

$$L_{loop}$$

the reduced loop-level inductance matrix,

$$M_{ij}$$

the mutual inductance between loop groups,

$$k_{ij} = \frac{M_{ij}}{\sqrt{L_{ii}L_{jj}}}$$

the coupling coefficient between loops, and

$$H(x, y, z)$$

the predicted magnetic near-field distribution above the PCB.

The script saves MATLAB result files for each configuration and exports CSV files containing loop self-inductance, mutual inductance, and coupling coefficient values. It also generates magnetic field magnitude and direction plots for both differential-mode and common-mode excitation cases. The exported model tag identifies the explicit two-winding common-mode choke model so that results from different model versions are not mixed.

## B.14 Modeling Assumptions and Scope

The MATLAB implementation is intended as a reduced-order, layout-aware electromagnetic model rather than a full-wave electromagnetic solver. The main assumptions are:

1. The EMI filter operates in the magnetoquasistatic regime, so retardation and far-field radiation effects are neglected.
2. Conductors are represented as thin straight filament segments.
3. Toroidal windings are approximated using stacked circular filament loops based on mean toroid diameter.
4. Magnetic cores are represented by calibrated effective permeability values instead of a full magnetic boundary solution.

5. Capacitor current paths are approximated as rectangular loop structures.
6. Near-field prediction is based on Biot–Savart superposition from solved loop currents.
7. AC conductor loss is approximated using a skin-depth-based resistance per unit length.
8. The model prioritizes layout comparison, coupling trends, and near-field behavior rather than full 3D solver-level detail.

These assumptions are intentional rather than merely limiting. They remove unnecessary full-wave complexity while retaining the dominant electromagnetic mechanisms needed for this thesis: layout-dependent inductive coupling, loop-to-loop interaction, and magnetic near-field variation. Because the operating regime is magnetoquasistatic, the reduced-order model provides accuracy comparable to a full-wave solver for the dominant magnetoquasistatic coupling quantities of interest, while offering faster setup, clearer physical interpretation, and more efficient configuration comparison.

## B.15 Summary of the Novel Contribution

The MATLAB implementation developed in this thesis provides a computationally efficient framework for connecting EMI filter layout geometry to circuit-domain coupling behavior and magnetic near-field prediction. The significant novelty is the combination of four features in a single reduced-order workflow:

1. Layout-aware geometry representation:

   Physical component locations, orientations, winding directions, and capacitor loop locations are retained.

2. Segment-level electromagnetic coupling:

   A MoM-style magnetoquasistatic kernel evaluates inductive interactions between current-carrying filament segments.

3. Loop-level circuit reduction:

   The large segment-level interaction matrix is aggregated into an interpretable loop-level inductance matrix.

4. Field reconstruction from circuit solution:

   Solved loop currents are mapped back to filament segments to predict magnetic near-field distributions above the PCB.

This creates a practical middle ground between lumped circuit analysis and full-wave electromagnetic simulation. The method is fast enough for configuration-level design comparison, but it still captures the dominant geometry-dependent inductive coupling mechanisms that influence EMI filter performance. This is the central methodological contribution of the thesis: a reusable, physically interpretable, and experimentally relevant modeling workflow for compact EMI-filter layout studies in the magnetoquasistatic regime.